Caroline Hiebl, BSc.

Li - Ion Transport in Mechanochemically Synthesized Garnets

MASTER´S THESIS

to achieve the university degree of

Diplom-Ingenieurin

Master´s degree programme: Technical Chemistry

submitted to

Graz University of Technology

Supervisor:

Univ.-Prof. Dr.rer.nat. Martin Wilkening

Institute for Chemistry and Technology of Materials

Graz, May 2017

Eidesstaatliche Erklärung

Affidavit

Ich erkläre an Eides statt, dass ich die vorliegende Arbeit selbstständig verfasst, andere als die angegebenen Quellen/Hilfsmittel nicht benutzt und die den benutzten Quellen wörtlich und inhaltlich entnommene Stellen als solche kenntlich gemacht habe. Das in TUGRAZonline hochgeladene Textdokument ist mit der vorliegenden Masterarbeit identisch.

I declare that i have authorded this thesis idependently, that i have not used other than the declared sources / resources, and that I have explicitly indicated all material which has been quoted eihter literally or by content from the used sources. The text document uploaded to TUGRAZonline is identical to the present master´s thesis.

…….. ……..

Datum/date **Unterschrift/signature**

Acknowledgement

I wish to thank Prof. Martin Wilkening for giving me the opportunity to do research in his working group. I also wish to thank Dipl.-Ing. Marlena Uitz for her guidance and the whole working group for their support. I would like to thank the Institute for Chemistry and Technology of Materials and the Federal Ministry for Science, Research and Economy as well as the Christian-Doppler Forschungsgesellschaft for making it possible to accomplish this work.

Abstract

Lithium ion batteries are indispensible in modern mobile applications. Besides being regarded as promising future storage system for green energy, safety aspects are of top priority of current research. The root of the safety issues associated with lithium ion batteries lies in the electrode materials used at present. Those are based on flammable non-aqueous liquid electrolytes. Irrespective of the risks they havent´t been replaced so far due to their high ionic conductivites. To overcome the hazard potential inorganic solid state electrolytes were proposed as suitable replacement. Garnet-type metal oxides are auspicious candidates because of their relatively high conductivities of 10^{-4} S cm^{-1} on average. In the following work the goal was to investigate the influence of aluminium doping levels and lithium concentration as well as sintering temperatures and holding times on the ionic conductivity and phase purity of $Li_7La_3Zr_2O_{12}$ (LLZO). Single step and mulitstep sintering procedures were performed. The ionic conductivities and acitvation energies were determined via electrochemical impedance spectroscopy (EIS) and the crystallinity and phases present were measured with X-ray powder diffraction (XRPD). Via electrochemical impedance spectroscopy predictions of the underlying origin of the ionic conductivity in different regions (e.g. bulk or grain boundary) of the samples could be made. The best results were achieved with $Li_{6.1}Al_{0.3}La_3Zr_2O_{12}$ + 0.375 Li_2O via single step sintering at 1000°C for 12 hours with a bulk conductivity of 6.51 x 10^{-6} S cm^{-1} at 20°C, an activation energy of 0.45 eV and a phase purity of over 97 vol % of cubic LLZO.

Kurzfassung

Lithium Ionen Batterien sind bei modernen tragbaren Geräten kaum mehr wegzudenken. Abgesehen davon, dass sie als vielversprechende zukünftige Speichersysteme für Ökoenergie angesehen werden, haben in der derzeitigen Forschung Sicherheitsaspekte höchste Priorität. Aktuell verwendete Elektrodenmaterialien sorgen für Sicherheitsbedenken in Zusemmenhang mit Lithium Ionen Batterien. Diese basieren auf entzündlichen, nicht-wässrigen, flüssigen Elektrolyten. Ungeachtet dieser Risiken wurden sie bisher aufgrund ihrer hohen Ionenleitfähigkeiten nicht ersetzt. Um dieses Gefahrenpotential beiseite zu schaffen wurden anorganische Festkörperelektrolyte als geeigneter Ersatz vorgeschlagen. Metalloxide auf Granatbasis sind vielversprechende Kandidaten aufgrund ihrer hohen Ionenleitfähigkeiten von durchschnittlich 10^{-4} S cm^{-1}. Das Ziel der folgenden Arbeit war es den Einfluss von Aluminium Doping Konzentration und Lithium Gehalt sowie Sintertemperatur und Haltezeiten auf die Ionenleitfähigkeit und Phasenreinheit von $Li_7La_3Zr_2O_{12}$ (LLZO) zu untersuchen. Es wurden ein- und mehrstufige Sinterprozesse ausgeführt. Die Ionenleitfähigkeiten und Aktivierungsenergien wurden mit Elektrochemischer Impedanzspektroskopie bestimmt und die Kristallinität und vorliegenden Phasen wurden mit Röntgenpulverdiffraktometrie untersucht. Mit Hilfe der Elektrochemischen Impedanzspektroskopie konnten Aussagen über den Ursprung der ionischen Leitfähigkeit verschiedener Regionen (z.B. Korn oder Korngrenzee) der Probe getroffen werden. Die besten Ergebnisse konnten mit $Li_{6.1}Al_{0.3}La_3Zr_2O_{12}$ + 0.375 Li_2O durch einstufiges Sintern bei 1000°C für 12 Stunden mit einer Kornleitfähigkeit von erreicht werden 6.51 x 10^{-6} S cm^{-1} bei 20°C, einer Aktivierungsenergie von 0.45 eV und einer Phasenreinheit von über 97 Vol% für kubisches LLZO erreicht werden.

Table of Contents

List of Abbreviations

c……cubic

DEC……diethyl carbonate

DME……..…dimethyl ethane

EC…… ethylene carbonate

EIS……electrochemical impedance spectroscopy

eV……...electronvolt

F…….. farad

LISICON……...…….lithium super-ionic conductor

LLZO……..$Li_7La_3Zr_2O_{12}$

MF……muffle furnace

NASICON…….sodium super-ionic conductor

PC……..……propylene carbonate

PEO……...polyethylene oxide

RT……...…room temperature

s……second

S…….siemens

SEI…….....……solid electrolyte interface

t…….……tetragonal

T……temperature

TF…….tubular furnace

V…….……..volt

vol%.....percentage by volume

wt%.....weightpercent

XR(P)D…….....….X-ray (powder) diffraction

1 Introduction

The continuously rising global demand for energy but concomitant depletion of fossil fuels and the request for environmentally benign energy sources spurred a great interest in green energy and suitable energy storage systems. Rechargeable lithium ion batteries are an attractive option for complimentary energy storage for renewable energy in mobile as well as stationary applications because of their high volumetric and gravimetric energy densities and high average cell voltage of 3.7 V.[1,2] The application range of lithium ion batteries covers not only portable devices such as laptops, smart phones or power tools, but also personal transportation, industrial, grid and stationary applications.[3]

The fundamental concept of a rechargeable lithium ion battery is a reversible intercalation process of the lithium ions into positive and negative host structures. The lithium ions are transferred between those electrodes via an electrolyte.[4] Because currently utilised lithium ion batteries contain liquid or polymer electrolytes with non-aqueous organic solvents, there are several safety issues associated with them that must be solved. They are flammable, have a poor electrochemical stability and the cells can leak and therefore impend health hazards on the user.[1,2]

Lithium ion batteries based on solid state electrolytes are promising candidates not only to overcome those problems but also offer new application possibilities. Among different classes of solid electrolytes for lithium ions like oxides, phosphates and sulfides[4], garnet-type metal oxides seem to offer the best advantages. Intensive and extensive research has stimulated significant efforts in the development of Li-stuffed garnet electrolytes[5] but there is still a long way to go until their commercialisation as sufficiently high lithium-ion conductivities have not been yielded yet via a feasible large scale production method.

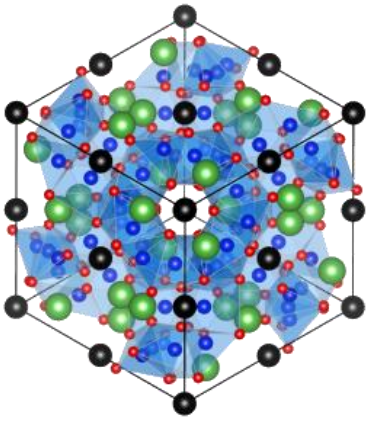

Figure 1 Crystal model structure of cubic garnet $Li_7La_3Zr_2O_{12}$, viewed along a <111> axis with La^{3+} (green), Zr^{4+} (black), Li^+ (dark blue),O^{2-} (red) and tetrahedral and octahedral sites for Li^+ ions (transparent blue).[6]

A tremendous amount of research was put into the synthesis of $Li_7La_3Zr_2O_{12}$, referred to as LLZO. This garnet-structured electrolyte is an attractive proposition for future battery applications due to its high thermal stability up to 900°C, stability against metallic lithium, air and moisture and the high ionic conductivity in the range of 10^{-3} to 10^{-4} S cm^{-1} at room temperature.[1,5,7–9] The synthesis of LLZO is delicate in terms of composition and temperature programs as processing plays a large role on the properties.[10] Unfortunately, there is currently no general rule how to modify the structure within one family of solid ion conductors due to missing profound knowledge about the processes in detail. Therefore, the optimum conducting species must be found by trial and error.[5]

Because only the cubic modification of LLZO with its formation temperature of 1230°C is of interest due to higher ionic conductivity than the tetragonal one, it is crucial to find ways to synthesise it at lower temperatures.[9] Doping with Al as well as Ga, Ta, Fe, Nb or Ba was found to stabilise the cubic modification at lower synthesis temperatures as it would not be stable at roomtemperature.[1,5,7–9] Aluminium stabilised garnet structured solid electrolytes are heavily researched on. Attention must be paid on alumina crucibles used during preparation at high temperatures due to additional Al uptake via diffusion into the garnet samples.[11]

In this work, aluminium stabilised LLZO samples were prepared according to two different synthesis paths. High energy ball milling and sintering temperatures ranging from 600 to 1200°C were involved. The aim was to achieve high ionic conductivities and low activation energies of pure cubic LLZO. Besides the different synthesis routes the samples differed in aluminium and lithium content. The structure and composition of the samples were measured via X-ray diffractometry. Electrochemical impedance spectroscopy was used to determine the ionic conductivities as well as activation energies.

2 Theoretical Part

2.1 Rechargeable Lithium Ion Batteries

2.1.1 Operation Principle of a Rechargeable Lithium Ion Battery

Battery cells come in a variety of shape designs like coin, cylindrical, prismatic and pouch cells.[12] A typical secondary lithium-ion battery is made of an intercalation cathode material, commonly a transition metal oxide, and a carbonaceous anode with a liquid or solid electrolyte in between the electrodes. The energy is electrochemically stored in the electrodes. After cell assembly, it is in the discharged state. For the charging process lithium ions are deintercalated from the cathode host structure and conducted via the electrolyte to the carbonaceous anode where they are incorporated. For charge neutrality, the electrons generated flow through an external circuit, where the charger and consumer are attached. Upon charging the energy can be retrieved via discharging by the reversed process via the external electron circuit.[12,13] In 1991 Sony commercialized the first-generation rechargeable lithium-ion cells with the following reaction mechanism[12]:

Cathode: $Li_{1-x}CoO_2 + xLi^+ + xe^- \underset{charge}{\overset{discharge}{\rightleftharpoons}} LiCoO_2$

Anode: $Li_xC_6 \underset{charge}{\overset{discharge}{\rightleftharpoons}} xLi^+ + xe^- + C_6$

Sum: $LiC_6 + CoO_2 \underset{charge}{\overset{discharge}{\rightleftharpoons}} C_6 + LiCoO_2$ E=3.7 V at 25°C

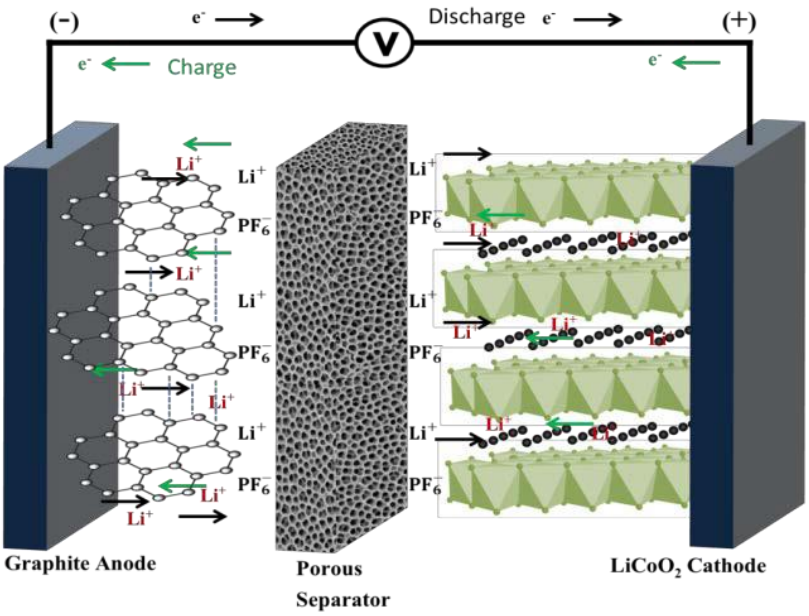

Figure 2Schematic of the main components of a Li-ion battery cell assembled in the discharged state[14]

2.1.2 Components

2.1.2.1 Cathode Materials

Since $LiCoO_2$ has been discovered as cathode material by Goodenough, much effort has been put into finding alternative options to replace this quite expensive material.[12] Those alternatives include for example the α-$NaFeO_2$ layer-structured materials $LiNiO_2$, $LiMn_xNi_yO_2$, $LiMn_xCo_yO_2$, $LiNi_xCo_yO_2$, $LiNi_xCo_yAl_zO_2$ or $LiNi_{1/3}Mn_{1/3}Co_{1/3}O_2$.[12,13] The main problem with those materials is the possibility of thermal runaway.[12] Another option are spinel-type $Li_xM_2O_4$ (M = Ti, V, Mn) materials.[12,13] Depending on x those cells can be either discharged at 4 V versus lithium ($0 \leq x \leq 1$) or at 3 V ($1 < x \leq 2$). At 4 V the cubic spinel structure remains unchanged during cycling whereas at 3 V it shifts to tetragonal symmetry. Because this impairs the battery life and performance another option is doping which results in $LiMn_{2-x}M_xO_4$ (M = Ni, Fe, Cr, Al, Co, Cu, or Li). Further research led to cost-effective nanosized $LiFePO_4$ positive cathodes and derivatives with a highly stable olivine structure[12].

2.1.2.2 Anode Materials

Up to now the only commercially utilized anode material in lithium ion batteries are lithiated carbons Li_xC_n. Carbonaceous materials, that can reversibly intercalate lithium, have different crystallinity and can be divided into soft and hard carbons depending on heat-treatment or graphitic and non-graphitic (disordered). Graphite can reversibly intercalate lithium ions without structural damage during cycling. LiC_6 has a potential of about 0 V against Li/Li^+ which means that the open circuit voltage is dependent on the cathode material of a cell. [12,13]

Additionally, a vast amount of research was put into finding suitable alloy anode materials as a substitution for graphite.

$$Li_xM \underset{charge}{\overset{discharge}{\rightleftarrows}} xLi^+ + xe^- + M$$

Lithium alloys with silicon and tin for example were thought to be promising candidates that offer higher capacities than graphite but they suffer from extreme volume changes up to 300 % during cycling. This leads to cracking of the cathode material and in the end to cell failure. Furthermore, lithium titanate ($Li_4Ti_5O_{12}$) was found to be a feasible structurally stable candidate with almost no side reactions.[12]

2.1.2.3 Separators

Even though the separator does not contribute to the electrochemical reaction in a liquid electrolyte battery cell itself, it is an important part of it helping to keep the electrodes apart and serving as electronic isolator but letting the ionic current through. These requirements can be met with a porous non-conductor. It is a microporous thin material made of a polymer or woven fabric that needs to be durable, (electro)chemically resistant and requires a high mechanical strength as well as wettability. Furthermore, separators also serve as security feature. Besides inhibiting dendrite formation on the anode leading to electronic bridging between the electrodes, they have a shutdown function in case of thermal runaway. In order to maintain a good battery performance, the material should not be too thick and appropriate pore sizes and distribution should lead to an uniform permeability. [12,13]

2.1.2.4 Electrolytes

Depending on the battery type there is a wide variety of electrolytes ranging from liquid, gel, solid polymer to inorganic solids available on the market place. Many requirements have to be met like high ionic conductivity and chemical stability over a wide temperature range, cost-effectiveness and they should not be-flammable or toxic which cannot easily be ensured as will be discussed later.[12] Not all processes taking place in energy storage devices are favourable and contributing. If those weren´t suppressed, cell failure would be the result. Not only the electrode materials themselves face unwanted reaction processes with the electrolyte, also current collectors made of aluminium do. Protection against this corrosion is a matter of the right choice of lithium salts and film-forming additives.[15]

2.1.2.4.1 Liquid Non-Aqueous Electrolytes

Liquid non-aqueous electrolytes must fulfil many requirements to be applied in lithium ion batteries. This can be achieved by blending several solvents together with an ion conducting salt and additives. Mixing different solvents and adding salts can change boiling and freezing points so that a broader liquid range is accessible. Ideally non-aqueous liquid electrolytes reach conductivities up to 10^{-2} S cm^{-1}. Unlike aqueous electrolytes they have a larger liquid range, better chemical stability and higher voltage windows but they lack of comparable conductivities, are costly and endanger the environment. In contrast to solid electrolytes they can manage small volume changes without losing contact to the electrodes and have higher conductivities.[15]

Generally, solvents are classified according to their dielectric permittivity ε and dynamic viscosity η. Typical solvents are for example diethyl carbonate (DEC), dimethyl ethane (DME), ethylene carbonate (EC), propylene carbonate or γ-butyrolactone (see figure 3).[15] Carbonate solvents are the first choice when it comes to liquid electrolytes because of their low viscosity

and stability window of 1.0-4.7 V versus Li^+/Li. The downside of carbonates is their high flammability.[12] Cyclic carbonates have high dielectric permittivity values but are more viscous. Therefore, linear carbonates with lower viscosity are added. The drawback are their low flashpoints (< 40°C) which lead to safety issues.[4]

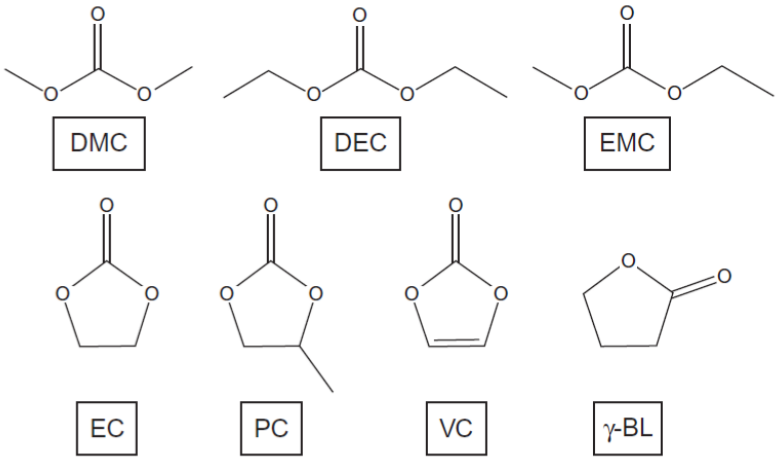

Figure 3 solvents for nonaqueous electrolytes - linear and cyclic carbonates[4]

The requirements for lithium salts range from (electro)chemical stability, low molecular weight, non-toxicity, affordability to the non-reactivity of the anion with other cell components.[15] In modern lithium-ion batteries $LiPF_6$ is used as salt. Although it is not the best salt its combination of various desirable properties makes it favourable. The downsides of $LiPF_6$ are its potential decomposition to HF, PF_5 and CO_2 when facing elevated temperatures and moisture.[4,12,15] Other salt options are $LiClO_4$, $LiBF_4$, $LiBC_4O_8$, $LiAsF_6$, $LiOSO_2CF_3$, $LiN(SO_2F)_2$ or lithium bis(oxalate)borate (LiBOB).[4,15]

2.1.2.4.2 Electrolyte Additives

As there is no perfect electrolyte known in the market place that meets all the needs of modern lithium ion cells additives provide improvement of their properties. An additive is an electrolyte compound over 5 % by weight or volume.[15] The aim is that electrolyte additives increase the safety without interfering with the cell components at the cost of the cell performance [4] Various types exist improving SEI formation, protecting cathodes, inhibit Al corrosion or suppress hydrolysis.[15] Also, agents for overcharge protection, improving the wettability of the separator, stabilizing $LiPF_6$ or flame retardants and many more are available.[4,15]

2.1.2.4.2.1 Solid Electrolyte Interface

As already mentioned above anode materials are made of carbon intercalation compounds, metallic alloys or spinel structures. Albeit the advantage of inhibited dendrite growth in contrast to pure lithium metal, carbonaceous materials can face irreversible parasitic reactions on the surface such as electrolyte decomposition and co-intercalations. Decomposition leads to passivating layers, so called SEIs (Solid Electrolyte Interfaces) which are permeable for Li^+ and hinder the reduction of the electrolyte by the electrode. If solvated lithium ions intercalate into the anode host material “exfoliation” is the result, which means cracking by volume expansion. SEIs build up in the first intercalation/deintercalation cycle. Besides the electrolyte and lithium salts also contaminants and additives contribute to SEI formation.[15]

2.1.2.4.2.2 Transference Numbers

The transference number describes the amount of the total ionic current that one ionic species carries through an electrolytic medium. It is defined as:

$$t_i = \frac{|i_i|}{\sum_i |i_i|}$$

where i_i is the fraction of the total ionic current carried by one species. [16]

2.1.2.4.2.3 Diffusion in Liquids

General description of diffusion by Fick´s first law:

$$J_i = -A * D \frac{\partial c_i}{\partial x}$$

with J_i… 1D flux, A … area across which diffusion occurs, D … diffusion coefficient, c_i…concentration, x … distance.

Stokes-Einstein-relation for estimation of diffusion coefficients in liquid electrolytes:

$$D = \frac{k_B T}{6\pi\eta r}$$

with k_B… Boltzmann´s constant, T … temperature, η… solvent viscosity, r… solute radius. Limitation: solute radius five times larger than the solvent radius.[15]

In aprotic liquid electrolytes, the ionic conductivity of the mobile species is modified via two main options. One is a higher dielectric constant of the solvent medium which leads to a better salt ion dissociation and the second option is reducing the viscosity. This can be seen in the Stokes-Einstein-relation. [5]

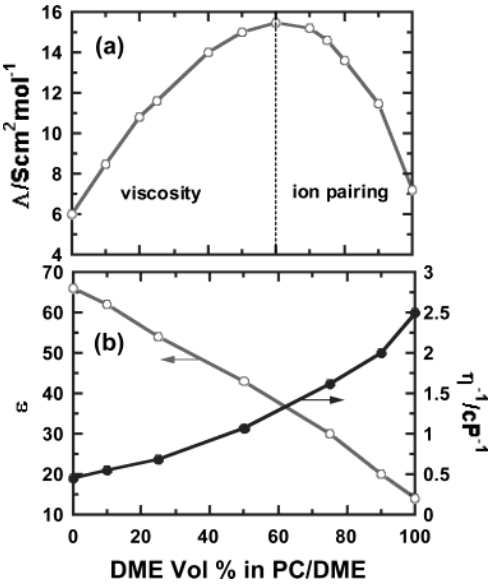

Figure 4 Dependency of the conductivity on the viscosity and dielectric constant in a solvent blend[17]

Figure 4 shows a solvent blend of dimethoxyethane (DME) and propylene carbonate (PC). With rising concentration of DME the viscosity of the mixture increases and the value of the dielectric constant decreases.[17] The upper diagram displays the conductivity trend of the blend. A high dielectric constant facilitates dissolving the lithium salt whereas a low viscosity favours fast ion transport through the electrolyte.[4] So, if the viscosity is too high as can be seen on the right side of the upper diagram, the result is ion pairing. For each solvent-salt blend there is a maximum ionic conductivity at a particular solvent ratio.

2.1.2.4.3 Polymer Electrolytes

Ionically conducting membranes, so called polymer electrolytes, are a type of solid state electrolyte applicable in lithium-ion batteries. They are polyether-based and albeit their conductivities are 1-2 orders of magnitude lower than liquid electrolytes the feasibility of making them very thin can outweigh this downside.[15] Solid electrolytes not only serve as ionic conductor but also as separator between the cathode and the anode in a battery cell. They are mostly polyethylene oxide (PEO) based and combined with lithium salts like $LiPF_6$, $LiAsF_6$ or lithiumbis(trifluoromethylsulfonyl)imide LiTFSI.[12] Generally, they can be divided into two different families:

2.1.2.4.3.1 Solvent-Free Polymer Electrolytes

The polymer must be capable of solvating salts. This depends on the coordinating groups as well as the chain length of the polymer and regarding the salt on its lattice energy. The ion transport itself has been found to mainly take place in the amorphous regions. So, the goal is to produce mostly amorphous polymers. This can be achieved by synthesising comb-branched polymers as for example crosslinked poly(methoxyethoxyethoxyphosphazene) “MEEP” and

block copolymers. The drawback of those electrolytes are the low conductivities below 10^{-4} S cm^{-1}at RT.[15]

2.1.2.4.3.2 Hybrid Electrolytes

To overcome this downside, combinations of polymers with other polymers, liquid or solid components, so called hybrid electrolytes are used. To solve the problems associated with liquid solvents and the low ionic conductivities of dry electrolytes, gel type electrolytes are investigated. They were developed to further increase the lithium ion conductivity by using plasticizers like PC, γ-butyrolactone or polyethylene glycol ethers which act as lubricants for the polymer chains.[12] This type of electrolyte consists of an immobilised liquid electrolyte either with a soluble polymer or in a microporous matrix.[15] It combines the properties of a plastic solid with the transport properties of a liquid.[4]

2.1.2.4.4 Inorganic Solid Electrolytes

It has been a long way since E. Warburg had discovered quasi pure ionic conductivity of some solid compounds in the nineteenth century to the growing interest of such materials as potential solid state electrolytes. The benefits of solid electrolytes are sole anionic or cationic conduction, the higher safety due to the absence of the possibility of leakage and no need for a separator. The design of solid electrolytes must be in accordance with various requirements such as high overall conductivity, optimal stability range, enhanced number and mobility of ionic defects and insignificant ionic contributions to the overall conductivity.[15] Liquid organic electrolytes have Li^+ transference numbers of about 0.2-0.5. Albeit solid state electrolytes have lower lithium ion conductivities than those, their Li^+ transference number close to 1 makes them quite comparable. A downside is the instability of some solid electrolytes concerning electrode materials.[5]

In search for comparable lithium-ion conductivities to those of liquid electrolytes, solids like NASICON, LISICON, argyrodites, perovskites, lithium halides and garnets look like an attractive proposition. Their structural families can be modified via doping and substitution and their conductivities are getting closer to those of liquid electrolytes. Unfortunately, currently there is no general rule how to modify the structure within one family of solid conductors due to missing profound knowledge about the processes in detail. Therefore, the optimum conducting species must be found by trial and error.[5]

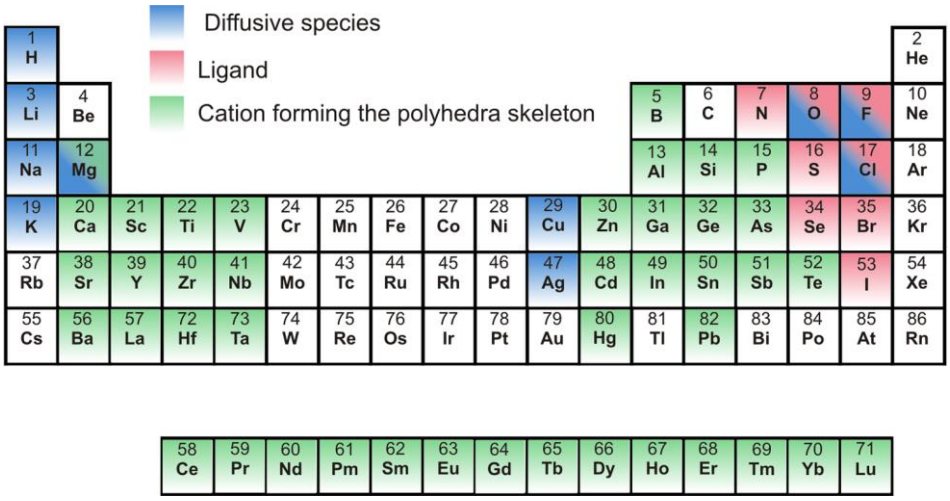

Figure 5 Periodic table for solid ionic conductors with diffusive species in blue, ligands in red and cations forming the polyhedra skeleton in green[5]

The most important factors for applicable solid state electrolytes are high ionic conductivities and thermodynamic stability. When it comes to charge carriers in solids multivalent ions do offer a higher charge transfer in contrast to monovalent ones but this is at the expense of their conductivity. Attention must be paid at the optimum size of the radii of the mobile ions for the present pathways.[15] There is a decline in ionic diffusion in crystalline solids with increasing valency of the mobile ions. For their radii, there is no similar discernible trend. They should neither not be too small nor too large with regard to the electrostatic forces and bottleneck sizes present in the lattice.[5] Another aspect is the activation enthalpy, which should be sufficiently low at ambient temperature.[15]

Enhancing the lithium ion conductivity of solid state conductors is possible via aliovalent substitution, which generates lattice defects like interstitials and vacancies. Nevertheless, this is limited so that the lithium ion conductivity goes through a maximum and decreases with increasing degree of substitution due to lattice distortions and hindered Li^+ diffusion. Grain boundaries limit ionic conduction due to a higher resistance than the bulk of a crystalline sample. This can limit the overall conductivity of a solid state electrolyte and the reduction of the grain boundary resistance is of special concern of research projects. [5]

2.1.2.4.4.1 Structural Defects and Diffusion in Solids:

The ionic conductivity of solid electrolytes is derived from structural defects and disorders in the crystal lattice.[18] If a considerable number of vacancies or interstitial ions exists, that leads to a disorder of a certain type of ions, high ionic conductivities can be realised in solid materials.[15]

In the case of a pure crystal the equilibrium defect concentration in case of a Schottky defect is defined as follows[18]:

$$n = N\ exp(-\frac{U}{kT})$$

with U…Energy of formation of a vacancy and N…number of anion and cation sites.

$$\Delta F = nU - T\Delta S$$

with ΔF…change in the free energy.[15]

Behind the movement of charge carriers in solids are several driving forces. Diffusion owing to a chemical potential gradient and migration due to an electric field are the major ones.[18]

Furthermore, the ionic transport in solid state electrolytes can be seen as statistical process of successive jumps between defect sites.[15,18] Diffusivity of a random motion in a 3D isotropic crystal:

$$D_i = \frac{1}{6}\ \nu r^2$$

with ν…jump frequency and r…jump distance. This allows an estimation of the maximum ionic conductivity.[15]

2.1.2.4.4.2 Preparation Methods

Principally the preparation methods can be divided into three main parts, the processes for monolithic samples, thick- and thin-film electrolytes.

Monolithic samples can be obtained for example from solid-state reactions, wet chemical methods and sintering processes. For solid-state reactions precursors such as oxides, hydroxides and carbonates are used. Prior to exposing them to a temperature program the starting materials are powder milled to the µm-range. Wet chemical methods on the other hand can achieve mixing on the atomic or molecular scale by mixing precursors with solvents. Thick-film electrolytes are produced via screen printing or tape casting whereas thin-film electrodes are made by sputtering, evaporation or spin-on coating.[15]

2.1.2.4.4.3 LISICON-like Electrolytes

LISICON is the abbreviation for lithium super ionic conductor. LISICON and thio-LISICON are based on the γ-Li_3PO_4 structure. The ionic conduction can be enhanced via substitution of P^{5+} by Si^{4+} or Ge^{4+}. Further substitution of O by S leads to thio-LISICON. [5]

2.1.2.4.4.4 NASICON-like Electrolytes

NASICON is the abbreviation for sodium super ionic conductor. The chemical formula is $L_{1+6x}M^{4+}_{2-x}M'^{3+}_{x}(PO_4)_3$ with L = Li or Na, M = Ti, Ge, Sn, Hf or Zr and M' = Cr, Al, Ga, Sc, Y, In or La where the MO_6 octahedra are corner sharing with PO_4 tetrahedra. [5] $Li_{1.3}Al_{0.3}Ti_{1.7}(PO_4)_3$ reaches total ionic conductivities of up to 7 x 10^{-4} S cm^{-1}.[15]

2.1.2.4.4.5 Argyrodite

The chemical formula is Li_6PS_5X with X = Cl, Br or I. They can reach ionic conductivities of up to 7 x 10^{-3} S cm^{-1} and small activation energies of 0.2-0.3 eV.[5]

2.1.2.4.4.6 Perovskite

The structure of perovskites is ABO_3 where Li^+ can replace the A-sites.[5] An example is $Li_{0.29}La_{0.57}TiO_3$ where lithium ions can diffuse through the crystal structure via a vacancy mechanism. $Li_{0.4}La_{0.51}TiO_{2.94}$ reaches a total ionic conductivity of 2-7 x 10^{-5} S cm^{-1}.[15] $La_{(2/3)-x}Li_{3x}TiO_3$ (LLT) has stability problems with elemental Li and Li alloys.[1]

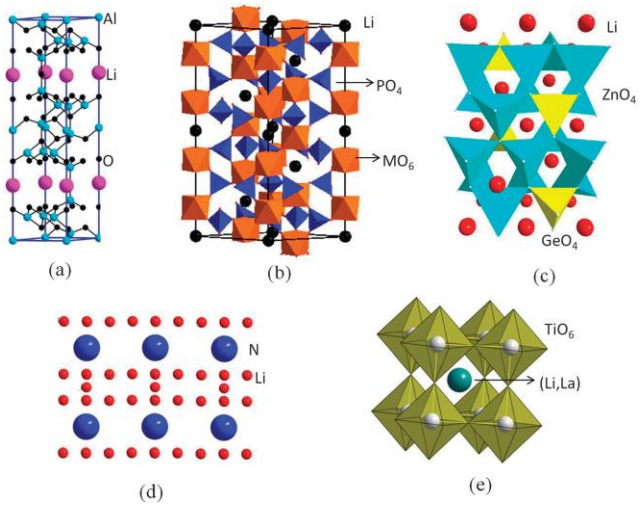

Figure 6 Structures of different Li^+-conductors: a) Li-β-alumina b) NASICON phosphate $LiM_2(PO_4)_3$ c) LISICON $Li_3Zn_{0.5}GeO_4$ d) Li_3N e) perovskite type $La_{(2/3)-x}Li_{3x}TiO_3$ [1]

2.1.2.4.4.7 Garnets

All lithium ion conducting garnets derive from the ideal garnet structure $A_3B_2(XO_4)_3$ with A = Ca, Mg, Y, La or rare earth and B = Al, Fe, Ga, Ge, Mn, Ni or V and X = Si, Ge, Al. A-sites are 8-fold, B-sites are 6-fold and X-sites are 4-fold oxygen coordinated cation sites. Lithium ions are located in the tetrahedral positions but to achieve higher Li-ion conductivities their concentrations must be increased e.g. by aliovalent substitution which leads to additional distribution over the distorted octahedral sites. Examples for lithium-ion conducting garnets are $Li_5La_3M_2O_{12}$ (M = Nb, Ta), which was studied by Thangadurai et al. in 2003 and reaches conductivities of 10^{-6} S cm^{-1} at RT, and derivatives like $Li_6ALa_2M_2O_{12}$ (A = Mg, Ca, Sr, Ba and M = Nb, Ta) or $Li_7La_3M_2O_{12}$ (M = Zr, Sn).[1,5,19]

The aim of the following work was to synthesise a lithium ion conductive $Li_7La_3M_2O_{12}$ garnet structure with M = Zr referred to as LLZO. This garnet-structured electrolyte is an attractive proposition for future battery applications due to its high thermal stability up to 900°C, stability against metallic lithium, air and moisture and the high ionic conductivity in the range of 10^{-3} to 10^{-4} S cm^{-1} at room temperature.[1,5,7–9] Murugan et al. was the first to study LLZO in the cubic structure as solid electrolyte in 2007.[20] The cubic modification is essential for a up to 2 orders of magnitude higher ionic conductivity than the tetragonal one and needs sintering temperatures as high as 1230°C (tetragonal: 980°C). Doping with Al as well as Ta, Fe, Nb or Ba stabilises the cubic modification at lower synthesis temperatures as it would not be stable at roomtemperature.[1,5,7–9] In the tetragonal modification, the litihium-ions are distributed over three different sites – a tetrahedral one (8a) and two distorted octahedral sites (16f and 32g).[1] In contrast to that the cubic polymorph has a disordered lithium ion distribution- over tetrahedral (24d) and octahedral (48g) sites as well as distorted 4-fold coordination (96h). [5,7] Rangasamy et. al investigated the influence of the Al-doping level as well as the Li-concentration in LLZO samples. He found out that there is a minimum of 0.204 moles and a maximum of 0.389 moles of aluminium necessary for successfully stabilising the cubic structure at 1000°C. The lithium concentration should range from 6.24 – 7.32 moles. One important point is to notice that if alumina crucibles are used for sintering, there is an aluminium uptake by the sample at elevated temperatures.[11] Recent research shows Ga^+ substitution as promising alternative to Al^{3+} showing Li^+ conductivities of 1.3 mS cm^{-1}.[7]

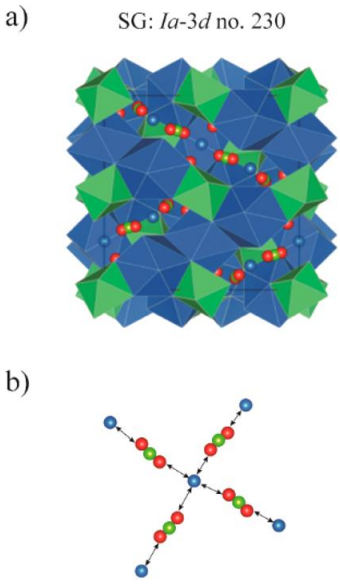

Figure 7 a) crystal structure of cubic LLZO; blue dodecahedra (La^{3+}), green octahedra (Zr^{4+}), Li^+ distributed over tetrahedral (blue spheres), octahedral (green spheres) and 4-fold coordinated sites (red spheres); b)Li^+ - diffusion pathway[21]

The synthesis of LLZO and derivatives is not straightforward. As mentioned above the best conducting garnets are found by trial and error. In literature one can find many different approaches ranging from various pre-treatments of the precursors, sol-gel synthesis[22], hot

press and spark plasma sintering to varying temperature programs for sintering via solid-state reaction routes[23] leading to a range of different room temperature conductivities and activation energies. Particularly important are the synthesis parameters such as temperature, time, doping level, sintering atmosphere and starting materials. Furthermore, an industrially feasible and inexpensive synthesis method is of crucial importance.[23] Attention must be paid to temperature and holding times as Li loss occurs at high temperature annealing.[24]

Düvel et al. synthesised Al-doped cubic LLZO via high-energy ball milling of the starting materials followed by a sintering step yielding a bulk conductivity of 10^{-4} S $cm^{-1}$and an activation energy of approximately 0.3 eV.[24] Xu et al. for example, proposed a multistep sintering method. Instead of heating the starting material up to a certain temperature, holding it and cooling it down to room temperature he suggested several heating steps. By this the sample has enough time to densify and attain the cubic modification. At 900°C the tetragonal modification of LLZO is formed and shifts to the cubic phase at 1100°C. For densification, the sample is heated up further to 1200°C. By using this method for samples doped with 0.2 mol% aluminium Xu et al. reached an ionic conductivity of 4.5* x 10^{-4} S cm^{-1} at RT.[23] Kumar et al. focused on the precursor preparation of a 2-step solid reaction method. A La-Zr-Al precursor was made by wet-ball milling, dried and put into a ethanolic solution of lithium acetate. After calcination pellets were sintered yielding in 1.6 x 10^{-4} S cm^{-1} at 293 K.[8]

2.1.3 Safety

Upon abuse of a battery system due to wrong charge/discharge or storage it can leak, vent or lead to explosions. Therefore, protective measures e.g. the battery management system, a positive temperature coefficient device (PTC), a current interruptive device (CID) and shutdown a separator are taken.[2,13] Events like overcharge, external and internal short and high temperatures can lead to dangerous situations. E.g. due to overcharge $LiCoO_2$ cathodes can decompose and oxygen is released.[2] Furthermore, especially liquid electrolytes with organic solvents such as alkyl carbonates (EC, DMC, DEC) have thermodynamic stability issues at the Li potential and are highly flammable. In addition, there are very toxic salts like $LiPF_6$. The P-F bond can be hydrolysed upon contact with tiny amounts of water leading to HF and POF_3.[15]

2.2 Used Methods and Techniques

2.2.1 Electrochemical Impedance Spectroscopy (EIS)

To optimise the development of new materials, powerful analytical tools like Electrochemical Impedance Spectroscopy (EIS) are needed to ensure maximum progress. With EIS as a non-invasive technique a wide scope of applications can be covered such as charge- and mass-transport measurements in energy storage systems and semiconductors or corrosion studies.[25] It is a versatile method allowing qualitative as well as quantitative assays using the frequency dependence of constituents for their separation.[10,26] For the right interpretation of the data it is crucial to know some specifications of the sample before the actual measurement.[25] With EIS sample properties like resistivity, conductivity or permittivity can be measured.

Besides the ideal resistor, where Ohm´s law can be applied, other circuit elements like an ideal capacitor exist. [25,27,28]

Ohm´s law:

$$R = \frac{V}{I}$$

with R…electrical resistance, V…input voltage and I…output current. [25]

The electrical resistance can be defined by the following formula if a uniform current passes through an ideally homogeneous sample located between two electrodes separated by the distance d with an area A is assumed while an external voltage is applied.

$$R = \rho \frac{d}{A}$$

with ρ [ohm/cm] …characteristic electrical resistivity of a material.[25]

Another circuit element mentioned above is the ideal capacitor. It can store the magnetic energy of an applied electric field, if two electrodes are separated by a dielectric medium. In contrast to an ideal resistor where AC current and voltage are “in phase” with each other, those signals are entirely “out of phase” in the case of an ideal capacitor.

Capacitance [F]:

$$C = \frac{\varepsilon_0 \, \varepsilon \, A}{d}$$

with ε_0 … constant electrical permittivity of vacuum and ε … relative permittivity of the medium.[25]

Impedance consists of a real (resistive) and an imaginary (capacitive) part and includes the phase differences between input voltage and output current.[10,25] In contrast to pure electrical resistance the imaginary component is used to describe the electrical energy that can be stored in a system. [25]

In an impedance experiment an AC sinusoidal voltage signal V with a small amplitude V_A at a frequency f is applied to an electrolyte between two electrodes.

$$V(t) = V_A \sin(2\pi f t) = V_A \sin(\omega t)$$

with V_A…amplitude [V], f…frequency [Hz], ω…radial frequency of the applied voltage signal [rad/s].[18,25]

The answer to the sinusoidal voltage input is a sinusoidal current response shifted in phase:

$$I(t) = I_A \sin(\omega t + \varphi)$$

with I_A… amplitude, ϕ…phase shift.[25,27] The phase shift for a pure capacitance it is π/2, a pure resistance 0 and for mixed cases the value lies in between.[27]

Complex impedance[25]:

$$Z^* = \frac{V(t)}{I(t)} = \frac{V_A \sin(\omega t)}{I_A \sin(\omega t + \phi)} = Z_A \frac{\sin(\omega t)}{\sin(\omega t + \phi)}$$

Euler´s relationship[25]:

$$\exp(j\phi) = cos\phi + jsin\phi$$

$$V(t) = V_A\, e^{j\omega t}$$

$$I(t) = I_A\, e^{j\omega t - j\phi}$$

$$Z^* = \frac{V}{I} = Z_A e^{j\phi} = Z_A(cos\phi + jsin\phi) = Z_{REAL} + jZ_{IM}$$

$$tan\phi = \frac{Z_{IM}}{Z_{REAL}}$$

at a chosen radial frequency ω.

Usually the frequency of the modulation is varied over a wide range (10^{-2} to 10^7 Hz).[10] The collected data of the measurement is represented in impedance spectra which usually show the absolute value of the impedance |Z| and the phase angle ϕ against the frequency ω. Different processes taking place in the sample all contribute to the total impedance. For better understanding it can be helpful to use circuit elements.[26]

Besides the complex impedance, other complex material properties as permittivity and modulus can be determined by EIS.

Debye Equation[25]:

$$P = (\varepsilon - 1)\varepsilon_0 V$$

with P…material polarization density cm/m^2 and V…applied electric field.

Complex permittivity- real and imaginary part:

$$\varepsilon^* = \varepsilon' - j\varepsilon''$$

with ε'…energy storage component and ε''…ionic conduction component.

$$\varepsilon' = \frac{Cd}{\varepsilon_0 A} \; and \; \varepsilon'' = \frac{d}{RA\omega\varepsilon_0} = \frac{\sigma}{\omega\varepsilon_0} = \frac{1}{\rho\omega\varepsilon_0}$$

Complex modulus[25]:

$$M^* = \frac{1}{\varepsilon^*} = M' - jM'' = j\omega\varepsilon_0 Z^*$$

$$M_{REAL} = -2\pi f \varepsilon_0 Z_{IM}$$

$$M_{IM} = 2\pi f \varepsilon_0 Z_{REAL}$$

Graphical Representation:

The impedance data can be represented in different ways. Diagrams as the Bode and Nyquist plots are helpful tools.

Bode:

A Bode diagram gives better insight into the frequency behaviour of the sample material. The phase angle ϕ and the logarithm of the absolute value of the impedance |Z| are plotted against the logarithm of the frequency log ω at the x-axis.[16,25,28]

Nyquist plot:

The Nyquist plot displays the real part of the impedance Z_{Real} on the x-axis and the imaginary part Z_{Im} with a negative notation on the y-axis for different values of the radial frequency ω.[25–28]

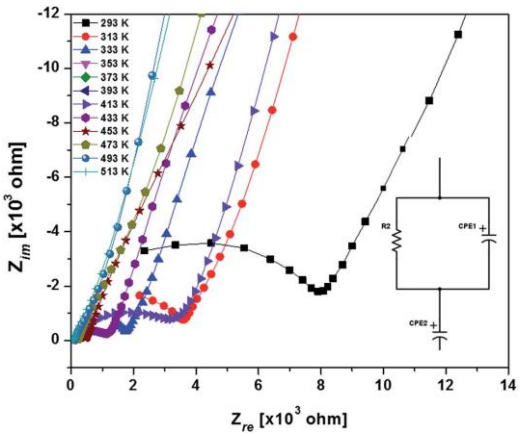

Figure 8 Nyquist plot of LLZO[8]

Various parts of a ceramic material can be characterised by a capacitance and a resistance in a parallel order.

Characteristic relaxation time of a parallel RC element:

$$\tau = RC$$

Frequency of maximum loss:

$$\omega_{max} RC = 1$$

Different RC elements of different regions in a sample can be treated separately. In a Nyquist diagram, each parallel RC element is displayed in a semicircle. From this one can determine the values of R and C. The value of R lies is the point of intersection of the semicircle with the x-axis and the value of C can be calculated. taking the frequency at the maximum of the semicircles into account. Via the capacitance values the responsible phenomenon (bulk, grain boundary) in the material is assignable (see figure 9). So, this measurement results help to determine the quality of sintering products and what phenomena contribute to the total resistance.[10]

Table 1Values of the capacitance and their possible responsible phenomena[10]

Capacitance [F]	Phenomenon Responsible
10^{-12}	bulk
10^{-11}	minor, second phase
$10^{-11} – 10^{-8}$	grain boundary
$10^{-10} – 10^{-9}$	bulk ferroelectric
$10^{-9} – 10^{-7}$	surface layer
$10^{-7} – 10^{-5}$	sample-electrode interface
10^{-4}	electrochemical reactions

Additionally, other representations like plotting the complex electric modulus M* give supplementary information if e.g. the grain boundary contributions dominate the total impedance in a Nyquist plot. In this case M´´ is plotted against the logarithm of the frequency log f.

$$M^* = j\omega\varepsilon_0 Z^*$$

with $C_0 = e_0 \frac{A}{l}$.

The impedance plot weights the most resistive elements the most whereas the electric modulus plot weights the elements with the smallest capacitance the most. Therefore, those two plots can look extremely different albeit displaying the same sample.[10]

2.2.1.1 Determination of the activation energy:

Relationship between σ_{ion} and T can be either derived from the diffusivity D or the mobility u assuming Arrhenius type behaviour[15]:

$$D = D_0 \exp(-\frac{E_a}{kT})$$

$$u = u_0 \exp(-\frac{E'_a}{kT})$$

D and u related by the Nernst- Einstein relationship[18]:

$$D = ukT$$

Arrhenius**:**

$$\sigma_{ion}T = (\sigma T)_0 \exp(-H\ \frac{E_a}{kT})$$

For determination of the activation energy σ_{ion}T versus 1/T plots used.[15]

2.2.2 X-Ray Diffraction (XRD)

To receive information on the structure and phases and properties like crystallinity of a solid sample X-ray diffraction can be utilized as reliable, non-destructive technique on powder samples.

X-rays have wavelengths in the range of 10^{-11} – 10^{-8} m. For laboratory use the generation of x-rays is realised with an X-ray tube and based on the photoelectric effect. Via an applied voltage high energy electrons are accelerated towards a metal target anode. The collision of the incident particles with the electrons of the target anode produces X-radiation. If the energy of the incident particle is higher than the binding energy of an electron to the nucleus of the metal

target, it will be ejected. An electron from an outer shell can fill up this vacancy producing fluorescent X-radiation characteristic for each metal target.[29]

Because the inter-atomic distances in crystal lattices are in the order of the wavelength of X-rays they act as three-dimensional diffraction gratings. A crystalline powder behaves like a single crystal that is rotated in different directions in space.[30] To understand the diffraction phenomena the Bragg equation was developed:

$$n\lambda = 2d_{hkl}sin\theta$$

with λ…wavelength of the waves, θ…angle between the incident wave and the surface plane and d…distance between the crystal planes. If n is a whole number, it results in constructive interference.

An X-ray beam hits a surface. The initial waves are in phase and are reflected from each plane of the crystal. The waves that hit the planes below the surface have a longer distance to travel. This leads them to be phase retarded in contrast to the wave reflected from the surface. If the additional distance (2 l) is a multiple of the wavelength λ it leads to constructive interference (= diffraction).[29]

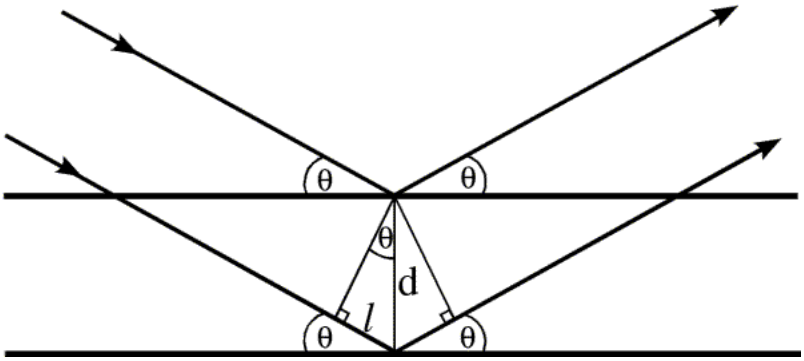

Figure 9 Bragg´s law[31]

For detection, a transducer and a pulse formation circuit are necessary. The former translates the X-ray photons into an electric current, which the latter converts into voltage pulses for further processing into a graphical representation of the intensities.[29]

3 Experimental Part

3.1 Mechanochemical Synthesis of $Li_7La_3Zr_2O_{12}$ (LLZO)

Two different methods were used for the synthesis of LLZO powders. The first one was a single step sintering procedure using dry milling for powder preparation by Düvel et al.[24] For the second method by Xu et al.[23] the LLZO powders were prepared by wet ball milling with subsequent multistep sintering.

3.1.1 Single Step Sintering

3.1.1.1 Powder Preparation

The first step in the mechanochemical synthesis of single step sintered LLZO was the preparation of a wide range of powder samples differing in Al-dopant content and Lithium excess by ball milling in a planetary ball mill (Fritsch Pulverisette 7). According to the following formula $Li_{7-3x}Al_xLa_3Zr_2O_{12}$ + 1.25 x Li_2O or 0.75 x Li_2O with x varying from 0 to 0.3, 2 g of each sample were weighed in with Li_2O (99.5%, Alfa Aesar), Al_2O_3 (99.99%, Sigma Aldrich), La_2O_3 (99.99%, Sigma Aldrich) and ZrO_2 (99%, Sigma Aldrich) as starting materials.

The powders were put into ZrO_2- grinding jars with 180 ZrO_2- grinding balls each and put into the planetary ball mill for 8 hours (15 min milling, 15 min pause, 32 cycles) at 600 rpm. After milling, the samples were removed from the jars with an alumina stick and ground with the help of an agate mortar. Prior to the sintering process pellets of about 90 mg and a diameter of 5 mm each were pressed for later characterisation with EIS.

3.1.1.2 Sintering

For sintering the mother powder and the pellets were put into alumina crucibles in the tubular furnace at a heating rate of 8°C per minute or into the muffle furnace at a heating rate of 10°C per minute. For comparison, a pellet of one sample (no. 6) was put on the mother powder and covered with it to determine the possible influence of the alumina crucible. Furthermore, sintering under argon was carried out in a quartz tube.

The parameters for temperature and holding time were set according to tables 2 and 3. After the individual holding times the samples were quenched to room temperature at 500°C.

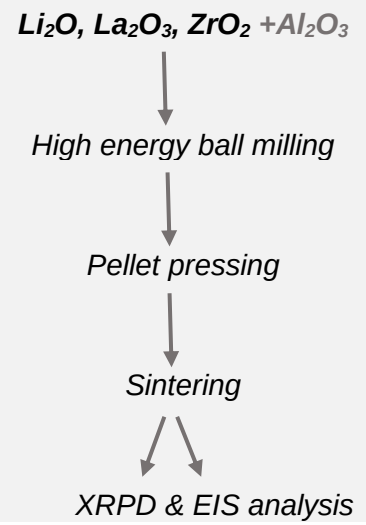

Figure 10 Scheme of Single Step Sintering

Table 2 Compositions and conditions for single step sintered LLZO samples in the tubular furnace

Single Step Sintering - Tubular furnace					
Sample Number	**x (Aluminium)**	**x Li_2O Excess**	**Temperature [°C]**	**Holding time [h]**	**Atmosphere**
1	0.3	0	milled only	0	0
2	0.3	0	600	6	air
3	0.3	1.25	600	6	air
4	0.3	1.25	1000	6	air
5	0.3	0.75	1000	6	air
6	0.3	1.25	1100	6	air
7	0	10 wt%	1100	6	air
8	0.2	1.25	600	6	air
9	0.2	1.25	1000	6	air
10	0.3	1.25	600	6	argon
11	0.3	1.25	1000	6	argon
12	0.2	1.25	1000	12	air
13	0.1	1.25	1000	6	air

Table 3 Composition and conditions for single step sintered LLZO samples in the muffle furnace

Single Step Sintering - Muffle furnace					
Sample Number	**x (Aluminium)**	**x Li_2O Excess**	**Temperature [°C]**	**Holding time [h]**	**Atmosphere**
14	0.3	1.25	1100	24	air
15	0.3	0.75	1100	24	air
16	0.3	1.25	1200	24	air
17	0.3	0.75	1200	24	air
18	0	10 wt%	1100	12	air
19	0.3	1.25	600	6	air
20	0.3	1.25	1000	12	air

3.1.2 Multistep Sintering

3.1.2.1 Powder Preparation

The first step in the mechanochemical synthesis of multistep sintered LLZO was the preparation of different powder samples. They differed in aluminium content and the temperature programme. La_2O_3 (99.99%, Sigma Aldrich), ZrO_2 (99%, Sigma Aldrich) and Al_2O_3 (99.99%, Sigma Aldrich) were dried at 900°C for 12 h in the tubular furnace and Li_2CO_3 (≥99.0%, Sigma Aldrich) was dried at 200°C overnight in vacuum. As for the single step sintered samples 2 g of each were prepared and milled with 5 ml of 2-propanol (99.5%, Sigma Aldrich) in the zirconia milling jars with 180 zirconia balls each at 600 rpm for 6 hours (15 min milling, 15 min pause, 24 cycles). The sample was washed out of the jars with approximately 10 ml of 2-propanol. The solvent was evaporated over time in a glovebox. The dried product was heated to 900°C for 12 h in the oven, reground at the same conditions as before and dried at 70°C overnight in vacuum. Prior to the sintering process pellets of about 90 mg and a diameter of 5 mm each were pressed for later characterisation with EIS.

Figure 11 Multistep Sintering Sample after evaporation of 2-propanol prior to 900°C heating step

3.1.2.2 Sintering

The sintering process of the mother powder and the pellets was carried out in a muffle (10°C min^{-1}) and tubular furnace (8°C min^{-1}) at different temperatures and holding times. As before, the samples were quenched to room temperature at 500°C.

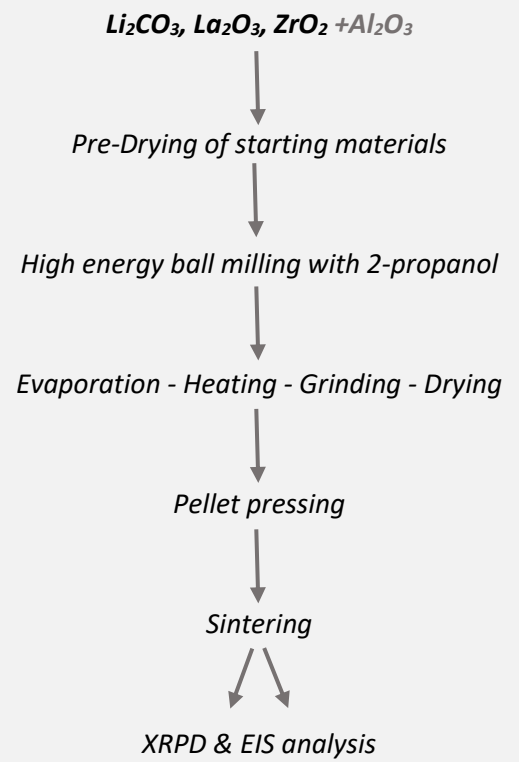

Figure 12 Scheme of Multistep Sintering

Table 4 Composition and conditions for multistep sintered LLZO samples in the muffle or tubular furnace

Multistep Sintering						
No.	**x (Aluminium)**	**x Li_2CO_3 Excess**	**Temperature [°C]**	**Holding time [h]**	**Atmosphere**	**Furnace**
21	0.3	1.25	900/1100/1200	6+6+12	air	muffle
22	0.3	1.25	600/1000	6+12	air	tubular
23	0.2	1.25	900/1100	6+12	air	tubular
24	0.1	1.25	900/1100	6+12	air	tubular

3.2 Characterisation of LLZO

3.2.1 X-Ray Powder Diffraction

In order to determine the crystallinity and phase composition of the powder samples X-ray diffractometry was used. The samples were measured with a Bruker D8-Advance X-ray powder diffractometer with a Lynexeye detector and Cu Kα-radiation. The scanning range was from 2θ = 10° – 100° with a step size of 0.02° and 2 s per step.

3.2.2 Electrochemical Impedance Spectroscopy

The ionic conductivity as well as the activation energy were determined via electrochemical impedance spectroscopy (broadband Novocontrol 80). For the measurements, the sample pellets were covered at the upper side and the bottom with a 100 nm thick layer of gold each serving as an electrical contact. Before the actual measurement the pellets were dried at 70°C overnight in vacuum. A temperature program (see table 5) from -100° to 200°C and a frequency range from 1.0 x 10^{7} Hz to 1.0 x 10^{-2} Hz was used.

Table 5 Temperature program of EIS

Temperature Program EIS							
	T [°C]		**T [°C]**		**T [°C]**		**T [°C]**
1	20	**11**	-20	**21**	20	**31**	180
2	40	**12**	-40	**22**	40	**32**	160
3	60	**13**	-60	**23**	60	**33**	140
4	80	**14**	-80	**24**	80	**34**	120
5	100 (held for 7200 s)	**15**	-100	**25**	100	**35**	100
6	80	**16**	-80	**26**	120	**36**	80
7	60	**17**	-60	**27**	140	**37**	60
8	40	**18**	-40	**28**	160	**38**	40
9	20	**19**	-20	**29**	180	**39**	20
10	0	**20**	0	**30**	200		

4 Results and Discussion

4.1 X-Ray Powder Diffraction

4.1.1 Single Step Sintering

4.1.1.1 Tubular Furnace

Figure 14 shows the XRD patterns of $Li_7La_3Zr_2O_{12}$ powders obtained from single step sintering in a tubular furnace that differ in aluminium doping levels and lithium content as well as sintering temperature. Sample number 1 did not undergo any temperature program and is completely amorphous. Therefore, high energy ball milling is not sufficient itself to form crystalline LLZO. A temperature treatment of 600°C for 6 hours leads to over 90 vol% of cubic LLZO and minor fractions of $La_2Zr_2O_7$, Li_2ZrO_3 and $LiLaO_2$ (see table 6). The pyrochlore structure $La_2Zr_2O_7$ is believed to form due to a lack of lithium.[11] So if excess lithium is added as in sample number 3, 100% cubic LLZO can be synthesised. Cubic LLZO is seen in the diffractogram by one well defined reflex at approximately $2\theta = 30.5°$.[11] Enhancing the temperature to 1000°C as in samples 4 and 5 leads to very similar products despite differing lithium concentrations. Further increase to a sintering temperature of 1100°C reduces the purity of the powder sample. Sample number 7 is a mixture of cubic and tetragonal LLZO as well as Li_2CO_3. No aluminium was added to this specimen. Albeit a sintering temperature of 1100°C the diffusion of aluminium out of the crucible was not sufficient to stabilise the cubic modification.

Table 6 XRPD results of single step sintered samples (1-7) in the tubular furnace

Single Step Sintering - Tubular furnace					
No.	**LLZO**	**$La_2Zr_2O_7$**	**Li_2ZrO_3**	**$LiLaO_2$**	**Li_2CO_3**
	[vol%]				
1	amorphous				
2	93 c	3.9	0.1	3	
3	100 c				
4	85.5 c	11.3	3.2		
5	88.5 c	11.4		0.1	
6	76.2 c	18.2			5.6
7	20.7 c & 58.2 t	12.1			9

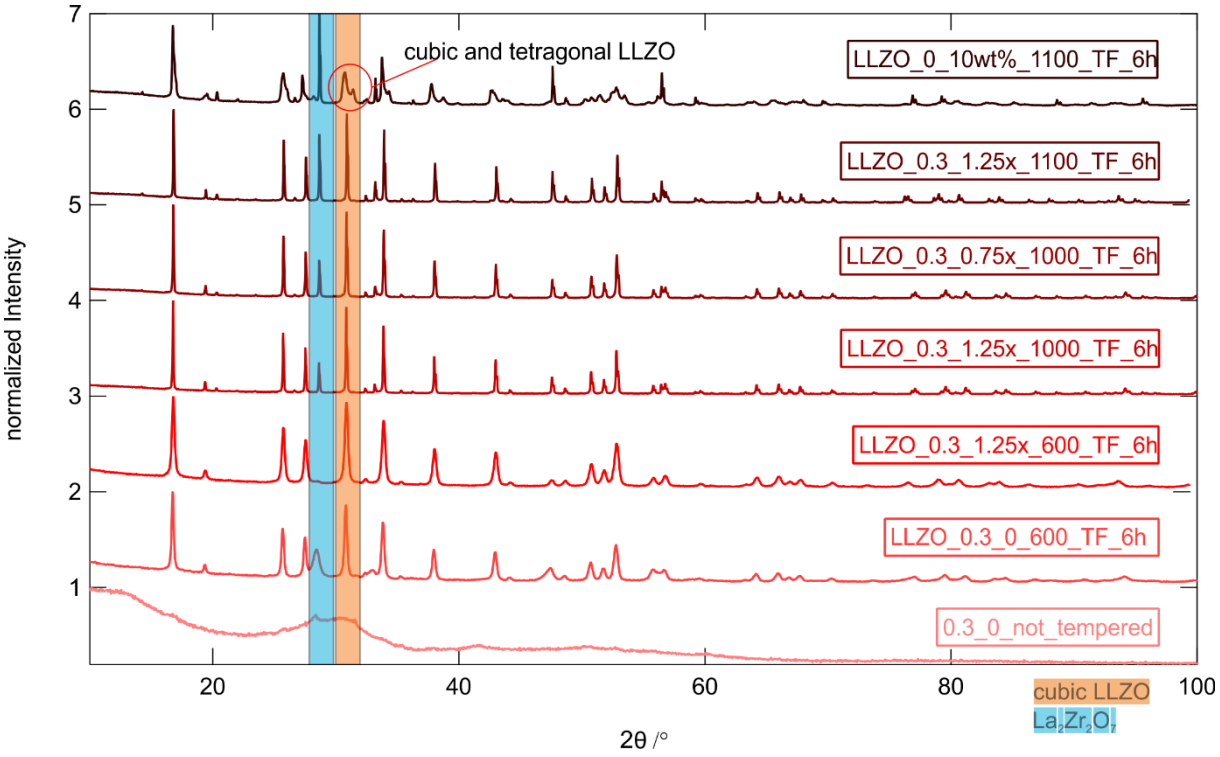

Figure 13 XRD pattern of $Li_7La_3Zr_2O_{12}$ with differing Al doping levels and Li concentrations obtained via single step sintering in the tubular furnace

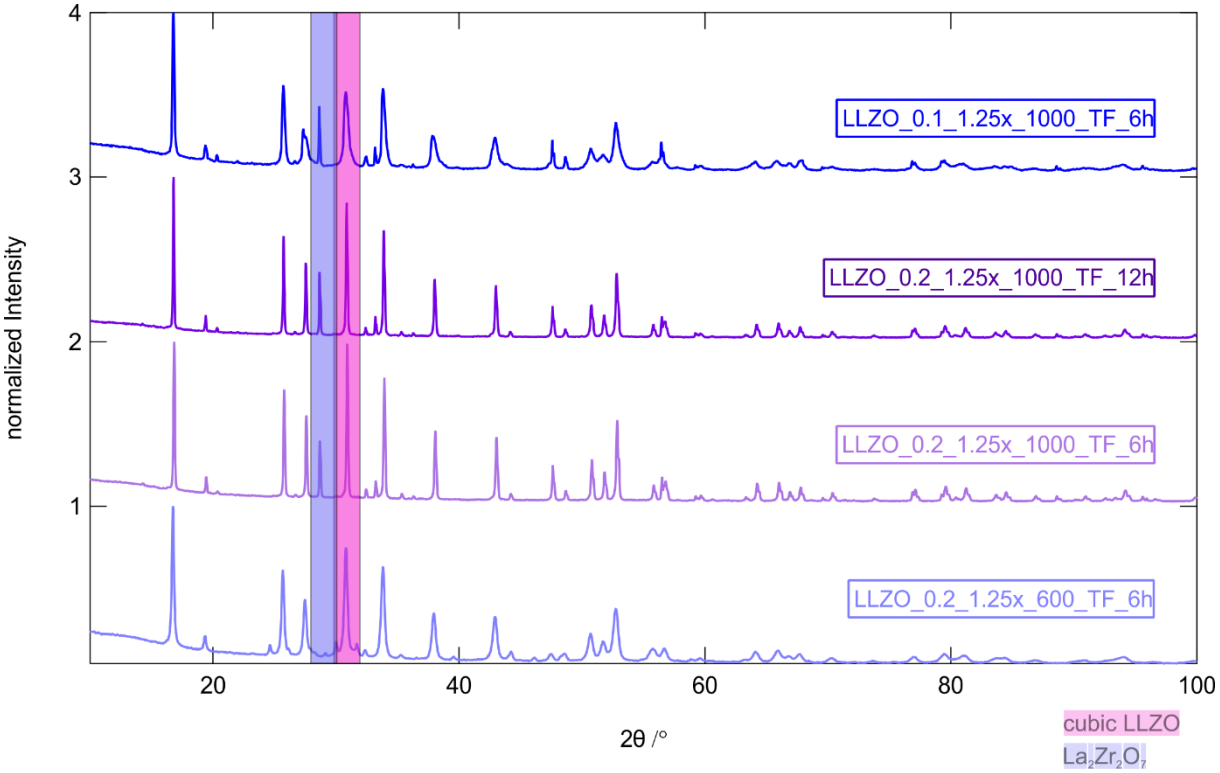

Figure 14 XRD pattern of $Li_7La_3Zr_2O_{12}$ with differing Al doping levels and Li concentrations obtained via single step sintering in the tubular furnace

In figure 15 XRD patterns of LLZO with lower aluminium doping levels as in figure 14 can be seen. Sample number 8 (x = 0.2) is a mixture of cubic and tetragonal LLZO as well as $LiLaO_2$ and Li_2CO_3. Enhancing the sintering temperature and time increases the amount of cubic LLZO

up to 99 vol%. A lower nominal aluminium concentration of x = 0.1 as in sample 13 does not significantly change the outcome.

Table 7 XRPD results of single step sintered samples (9-13) in the tubular furnace

Single Step Sintering - Tubular furnace				
No.	**LLZO**	**$La_2Zr_2O_7$**	**$LiLaO_2$**	**Li_2CO_3**
	[vol%]			
8	69.7 c & 21.6 t		0.9	7.8
9	91.1 c	8.9		
12	99 c	1		
13	89 c	11		

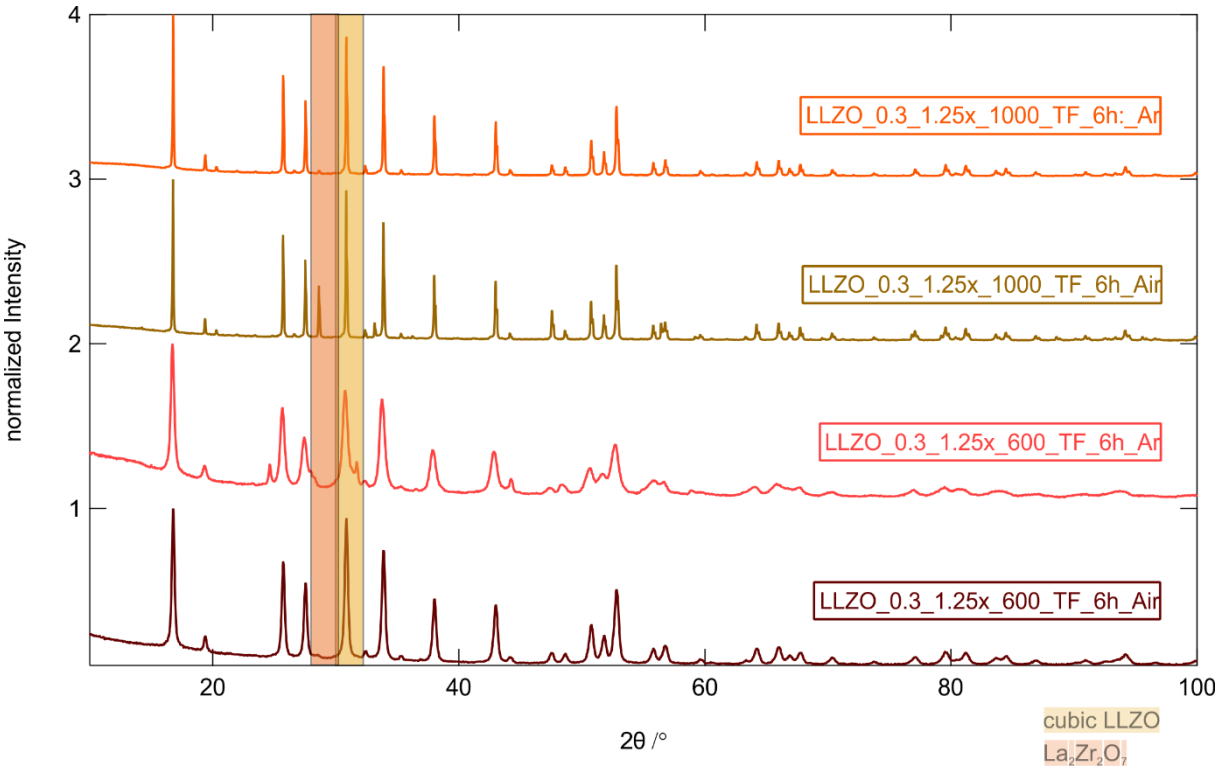

Figure 15 XRD pattern of $Li_7La_3Zr_2O_{12}$ with differing Al doping levels and Li concentrations obtained via single step sintering in the tubular furnace

Figure 16 compares the XRD data of the powders sintered under atmospheric conditions and argon with nominal aluminium content of x = 0.3 at 600°C and 1000°C ($Li_{6.1}Al_{0.3}La_3Zr_2O_{12}$ + 1.25 x Li_2O). Despite having the same composition, samples sintered under argon show the opposite trend regarding cubic LLZO content as samples sintered under atmospheric conditions. Under Argon higher temperatures are needed to reach phase pure cubic LLZO. Sample number 11 shows 100 vol% of LLZO in the cubic modification. As can also be observed in figures 13 and 14 the width of the reflexes decreases with increasing temperature indicating grain growth. This is favoured as grain boundaries limit ionic conductivity.

Table 8 XRPD results of single step sintered samples (3, 4, 10, 11) in the tubular furnace

Single Step Sintering - Tubular furnace			
No.	**LLZO**	**$La_2Zr_2O_7$**	**Li2ZrO3**
	vol%		
3	100 c		
4	85.5 c	11.3	3.2
10	90 c	10	
11	100 c	0	

4.1.1.2 Muffle Furnace

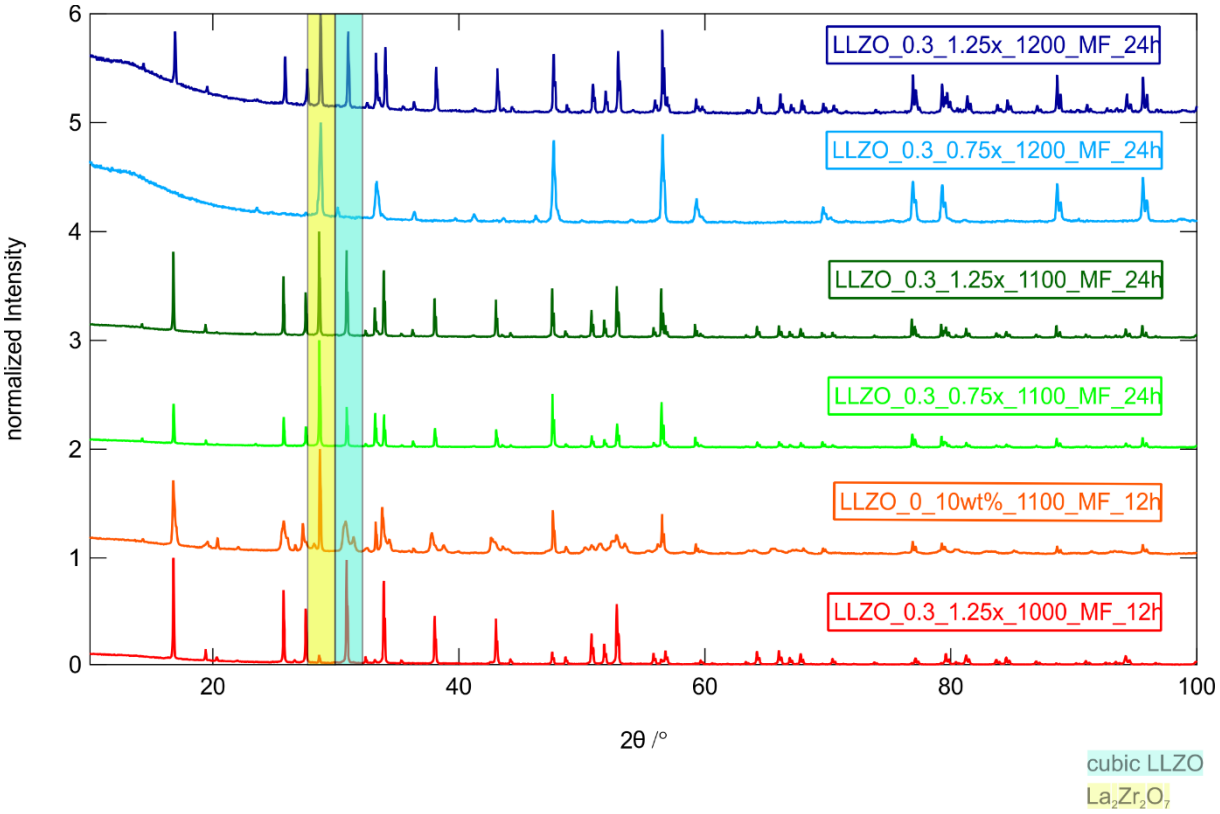

Figure 16 XRD pattern of $Li_7La_3Zr_2O_{12}$ with differing Al doping levels and Li concentrations obtained via single step sintering in the muffle furnace

The XRD patterns of the samples sintered via single step sintering in the muffle furnace are presented in Figure 17. Among those samples the one sintered at 1000°C for 12 h shows the best results with very low levels of impurities. With rising sintering temperature, the amounts of cubic LLZO decrease. The main impurity phase is $La_2Zr_2O_7$, which constitutes 87.4 vol% of sample number 17. This can be assigned to a lack of lithium reaching a critical concentration due to the high temperature of 1200°C for 24 hours. Sample number 18 without aluminium doping is a mixture of cubic and tetragonal LLZO as well as impurities of $La_2Zr_2O_7$, Li_2ZrO_3 and $LiLaO_2$.The absence of aluminium doping does not stabilise the cubic structure even at 1100°C.

Table 9 XRPD results of single step sintered samples (14-20) in the muffle furnace

Single Step Sintering - Muffle furnace						
No.	**LLZO**	**$La_2Zr_2O_7$**	**Li_2ZrO_3**	**$LiLaO_2$**	**Li_2CO_3**	**La_2O_3**
	[vol%]					
14	63.7 c	35.8	0.5			
15	57.5 c	38.5			3.8	
16	61.7 c	32.6	2.7		3	
17	2.9 c	87.4	9.7			
18	37.6 c & 40.4 t	16.4	5.3	0.2		
19	97.7 c	0.2	0.5		1.8	
20	97.25 c	2.7				0.05

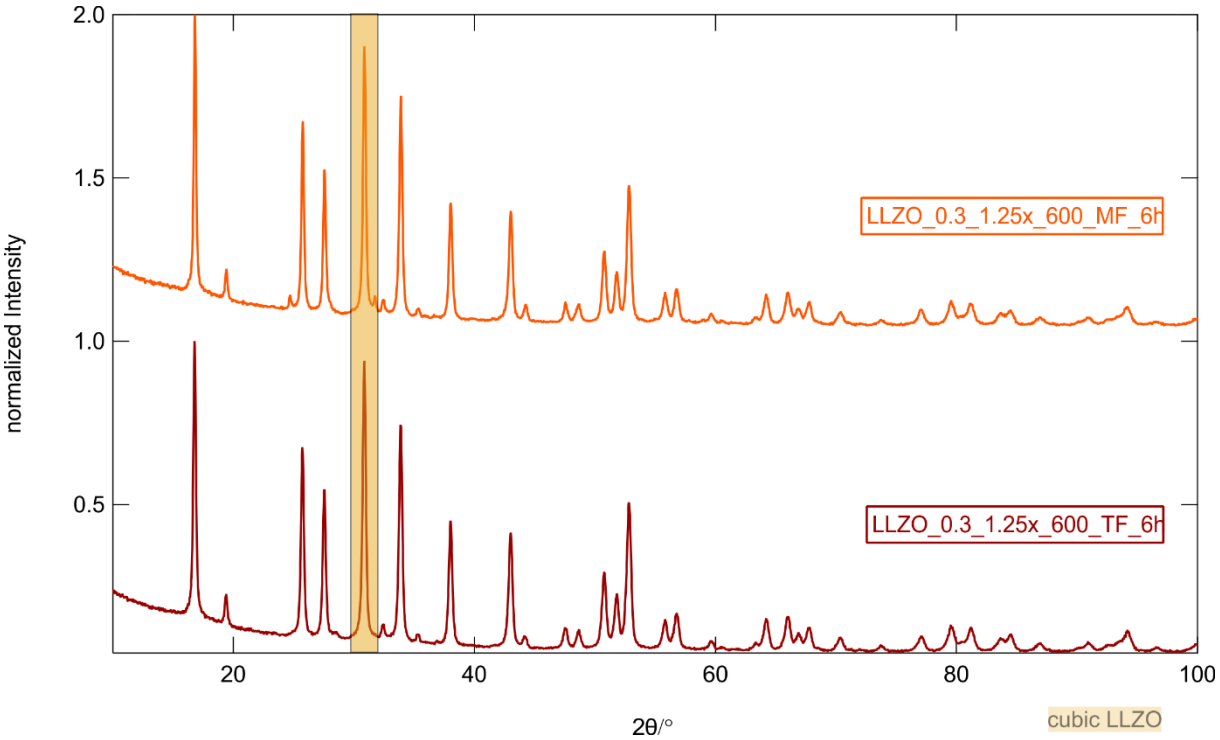

Figure 17 comparison of the XRD pattern of $Li_{7-3x}Al_xLa_3Zr_2O_{12}$ + 1.25 x Li_2O with nominal Al^{3+} concentration of x = 0.3 obtained via single step sintering in the muffle and tubular furnace at 600°C

The experimental data and results of the XRD measurements of sample 3 and 19 are presented in figure 18 and table 10. So far the best results have been achieved with $Li_{6.1}Al_{0.3}La_3Zr_2O_{12}$ + 1.25 x Li_2O sintered at 600°C for 6h. The powder that was subjected to the temperature treatment in the muffle furnace shows traces of 0.2 vol% $La_2Zr_2O_7$ and 0.5 vol% Li_2ZrO_3.

Table 10 Comparison of XRPD results of single step sintered samples (3 and 19) in the tubular and muffle furnace

Single Step Sintering				
No.	**LLZO**	**$La_2Zr_2O_7$**	**Li_2ZrO_3**	**Li_2CO_3**
	[vol%]			
3 (TF)	100 c			
19 (MF)	97.7 c	0.2	0.5	1.8

4.1.2 Multistep Sintering

Sample number 21 sintered via a 3-step temperature program in the muffle furnace could not be analysed as it was so firmly attached to the alumina crucible and could not be removed anymore.

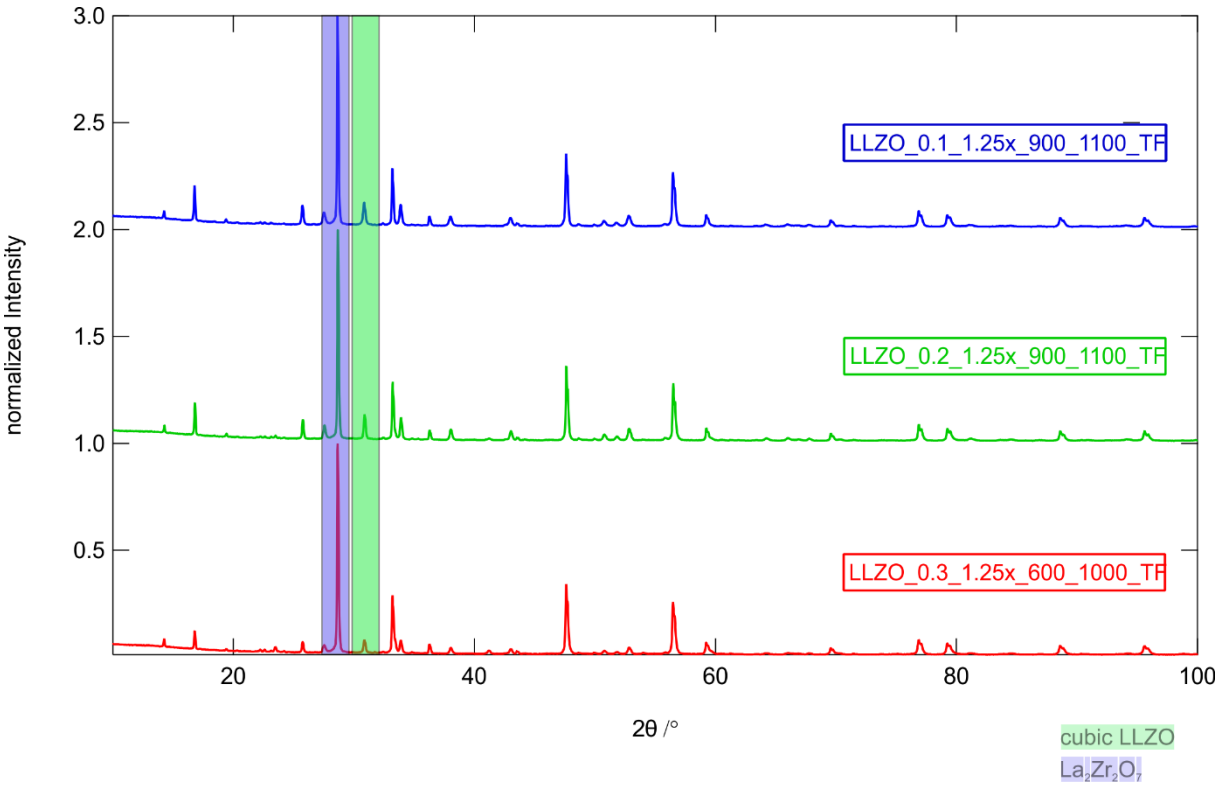

Figure 18 XRD pattern of $Li_7La_3Zr_2O_{12}$ with differing Al doping levels and Li concentrations obtained via multistep sintering in the tubular furnace

Figure 19 shows the XRD pattern of the multistep sintered samples with varying aluminium content. Sample 22 with a nominal aluminium content of x = 0.3 sintered at 600° and 1000°C consisted of 21 vol% cubic LLZO and 79 vol% $La_2Zr_2O_7$.By lowering the aluminium doping level and increasing the sintering temperature as in samples 23 and 24 the content of the cubic modification could be raised to over 30 vol%. For all three samples the reflection for the cubic modification of LLZO can be observed at 2θ = 30.5°.

Table 11 XRPD results of multistep sintered samples (22-24) in the tubular furnace

Multistep Sintering – Tubular furnace		
No.	**LLZO**	**$La_2Zr_2O_7$**
	[vol%]	
22	21 c	79
23	32 c	68
24	34 c	66

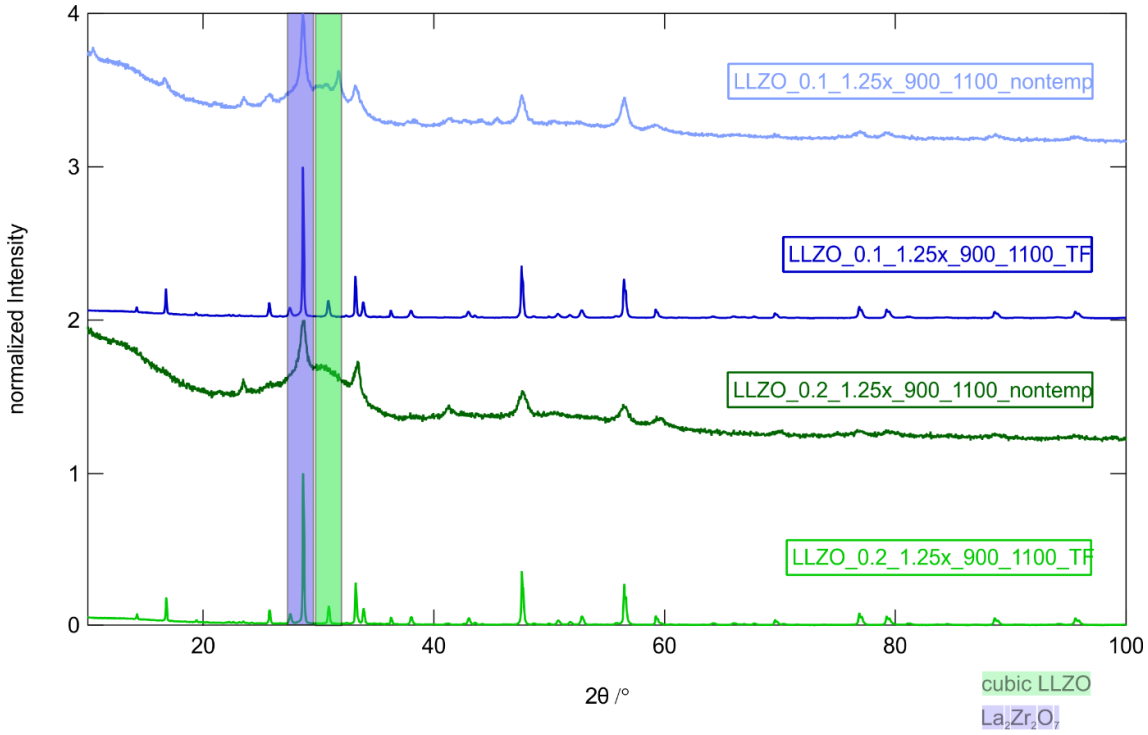

Figure 19 Comparison of the XRD pattern of $Li_7La_3Zr_2O_{12}$ with differing Al doping levels and Li concentrations obtained pre-sintering and via multistep sintering in the tubular furnace

Because the precursor powders for the multistep sintering method did undergo a heat-treatment at 900°C before the actual sintering process, they were measured via X-ray diffractometry to see if this was sufficient for the formation of cubic LLZO. As can be seen in figure 20 and table 12 this pre-treatment does primarily lead to $La_2Zr_2O_7$.Furthermore, the width of the reflexes is very broad indicating bad crystallinity.

Table 12 Comparison of XRPD results of multistep sintered samples (23 and 24) before and after sintering in the tubular furnace

Multistep Sintering - Tubular furnace		
No.	**LLZO**	**$La_2Zr_2O_7$**
	[vol%]	
23	32 c	68
23 before tempering		100
24	34 c	66
24 before tempering	12 c	88

4.2 Electrochemical Impedance Spectroscopy

After the XRD measurements the ionic conductivities and activation energies of the samples with the highest content of cubic LLZO were determined via electrochemical impedance spectroscopy. In order to investigate the influence of the aluminium content as well as the sintering temperature on the conductivity performance of the synthesised LLZO samples, they were analysed by using different plots. Below the results of the single step as well as the multistep sintered samples are presented in diagrams and summarized in tables and compared to each other.

As already mentioned in the theoretical part of EIS, the received conductivity values of the impedance measurement can be assigned to e.g. the bulk or grain boundary regions via their characteristic capacitance values. (see table 1) Those capacitance values can be obtained using Nyquist plots as shown below with sample number 20.

4.2.1 Single Step Sintering

No. 20 – LLZO_0.3_1.25x_1000_MF_12h:

Figure 21 shows the ionic conductivity of sample number 20 plotted against the frequency. The colours indicate the different temperatures starting at the bottom with – 100°C in dark blue to 200°C in orange on the top. Three distinct plateaus can be seen at each temperature. In order to determine the activation energies in these regions a straight line was drawn and the points of the intersection with the individual curves were used for calculation (the plot for the third plateau can be seen in figure 22). The logarithm of the conductivity times the temperature was plotted against the inverse temperature. After fitting the curve the activation energy was calculated for the bulk region to be 0.45 eV and its ionic conductivity is 6.51 x 10^{-6} S cm^{-1} at 20°C. To be able to assign the conductivities to the different regions (bulk or grain boundary) a Nyquist diagram was made by plotting the negative of the imaginary impedance against the real part of the impedance at 20°C.

$$\omega_{max} * R * C = 1$$

with $\omega_{max} = 2\pi f$

ω_{max} can be calculated by taking the value of the frequency at the maximum of one semicircle and R is the value of real impedance at the point of intersection at the x-axis shown in diagram 23. With the value of the capacitance C (see table 1) the region can be determined. In this case, it was in the order of 10^{-12} F (bulk region). Figure 24 shows the temperature dependence of the ionic conductivity. Table 13 summarises all obtained values for bulk and grain boundary ionic conductivities as well as activation energies at 20°C.

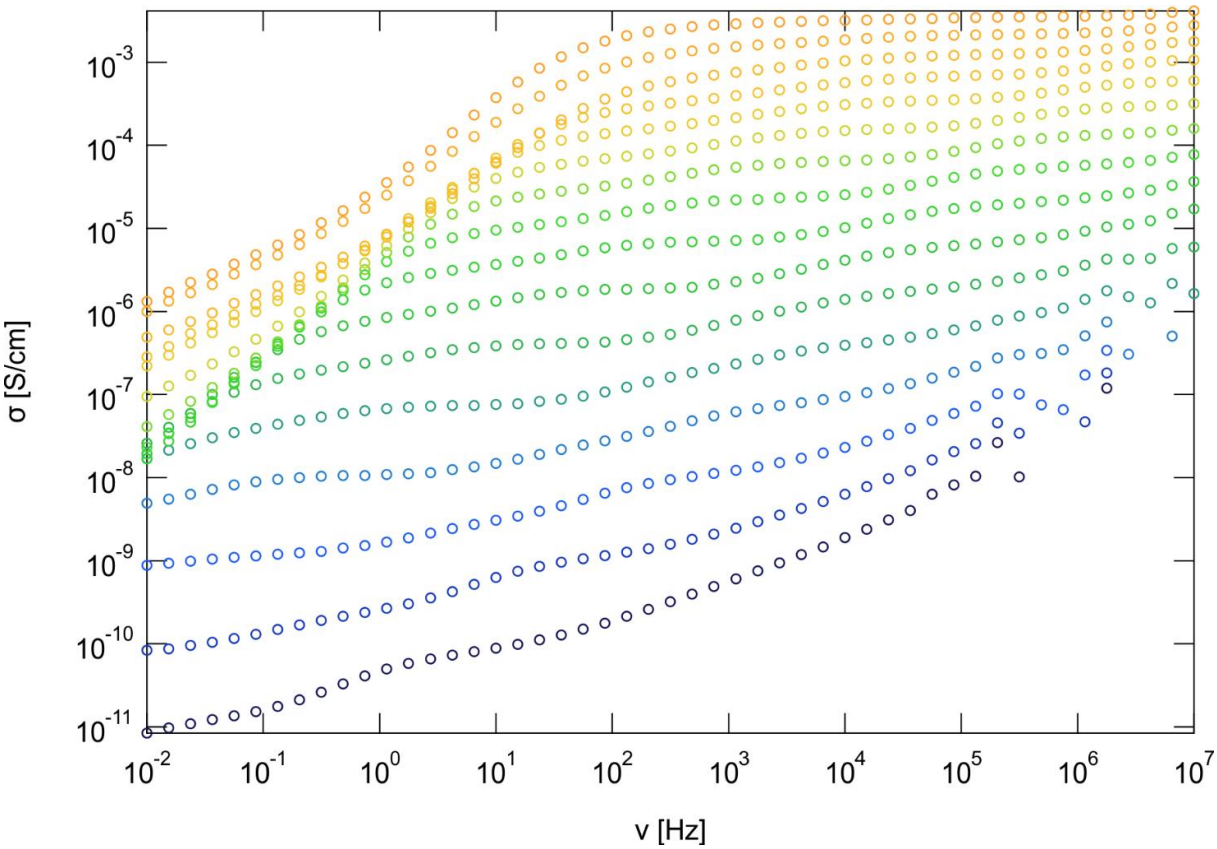

Figure 20 Conductivity plot of sample number 20 showing three plateaus

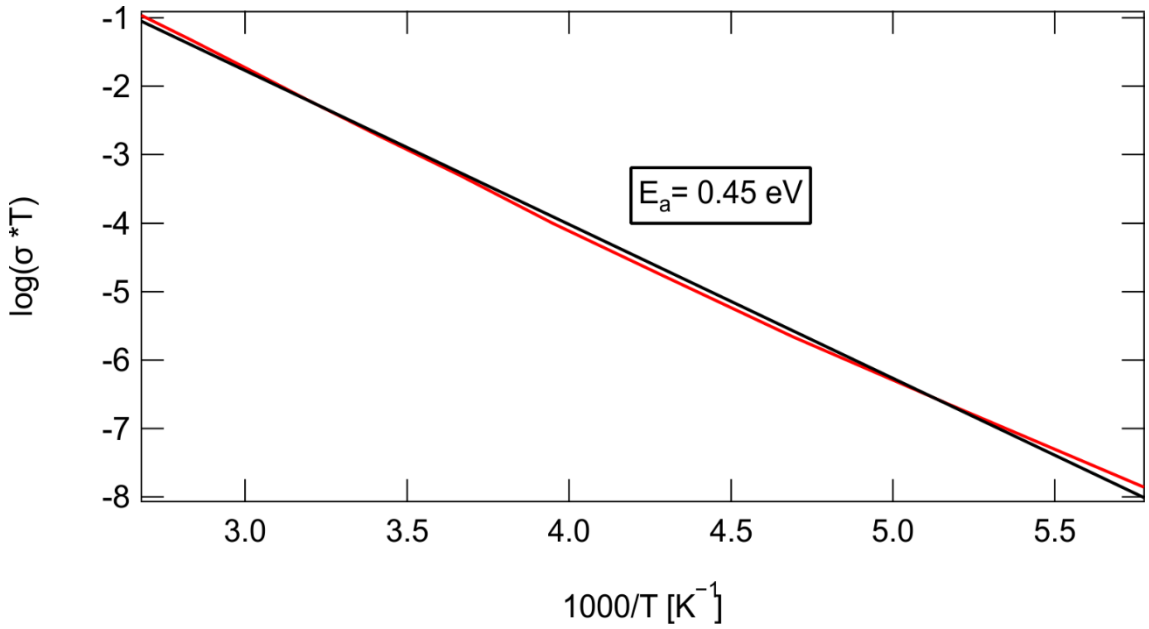

Figure 21 Arrhenius plot of sample number 20 showing the activation energy of the bulk region

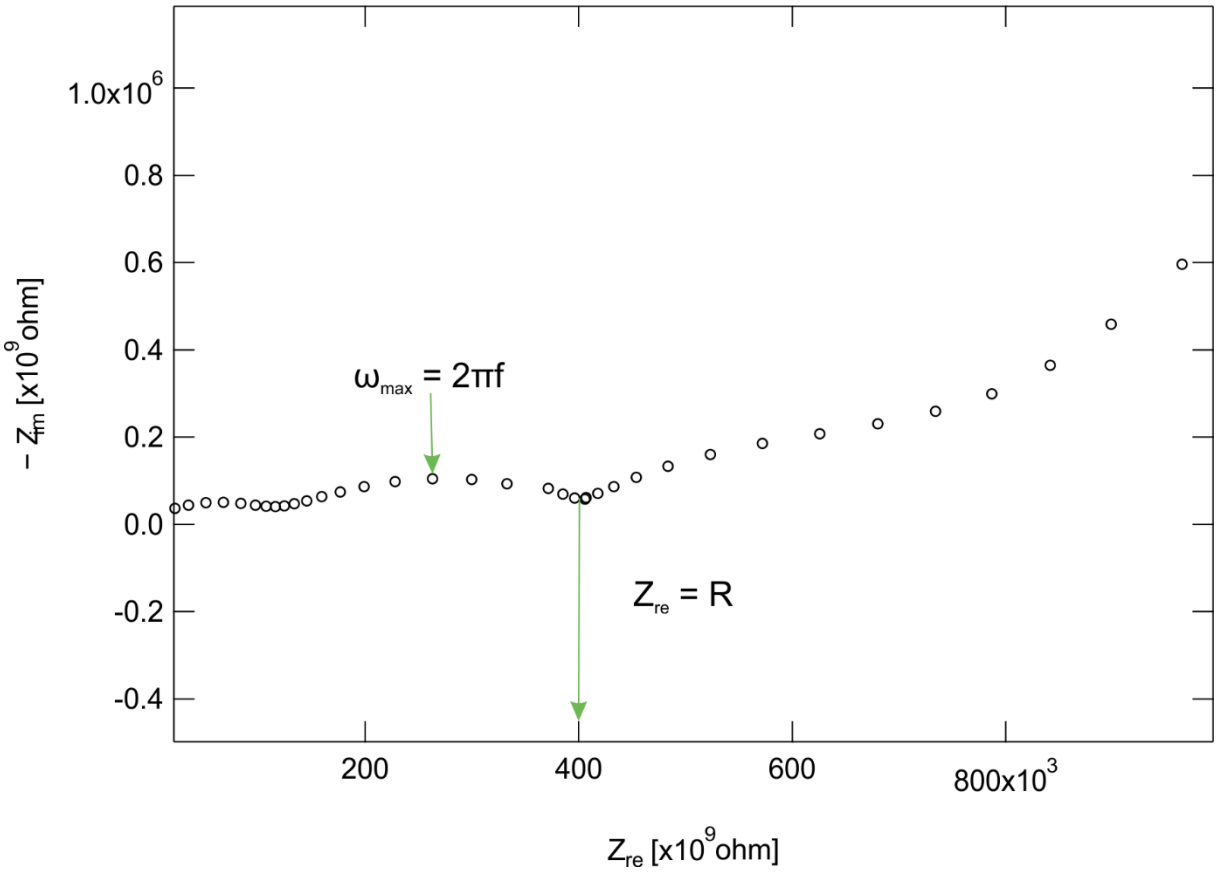

Figure 22 Nyquist plot at 20°C for sample number 20 showing three semicircles

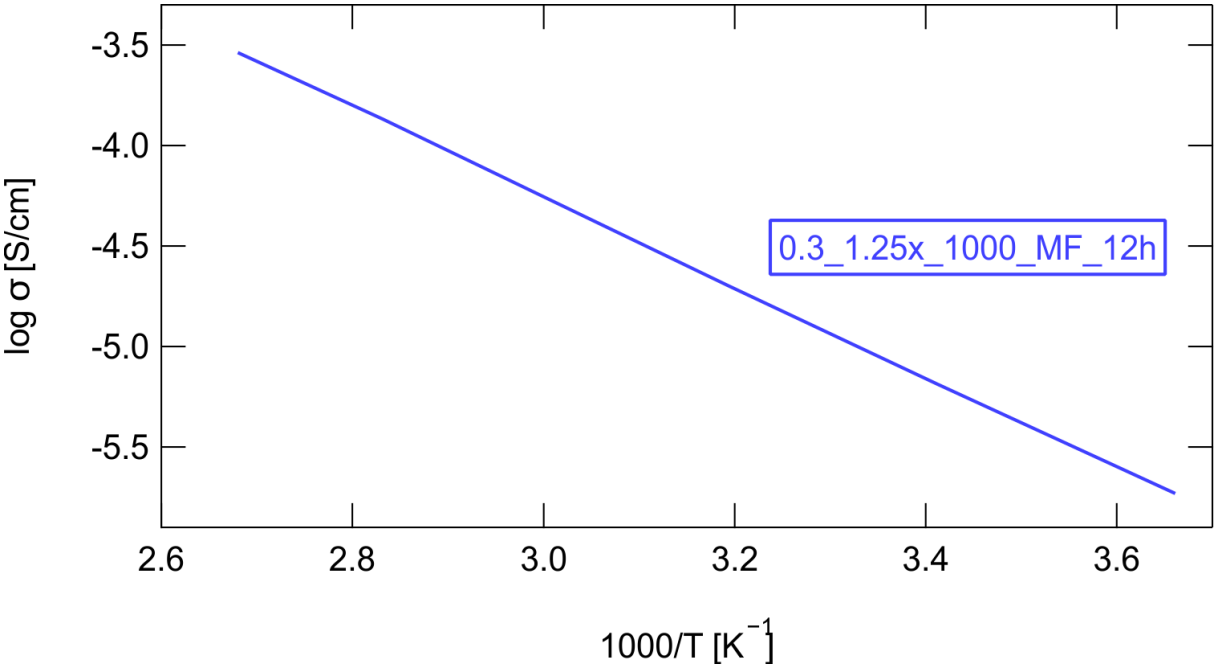

Figure 23 Temperature dependent bulk conductivities for sample number 20

No. 3 – LLZO_0.3_1.25x_600_TF_6h and no. 19 – LLZO_0.3_1.25x_600_MF_6h:

Via XRD measurements sample number 3 and 19 were confirmed to be in the cubic modification of LLZO (100 vol% and 97,7 vol%). Nevertheless, EIS measurements show low ionic conductivities and high activation energies for the grain boundary regions of both samples (see table 13, figure 25).

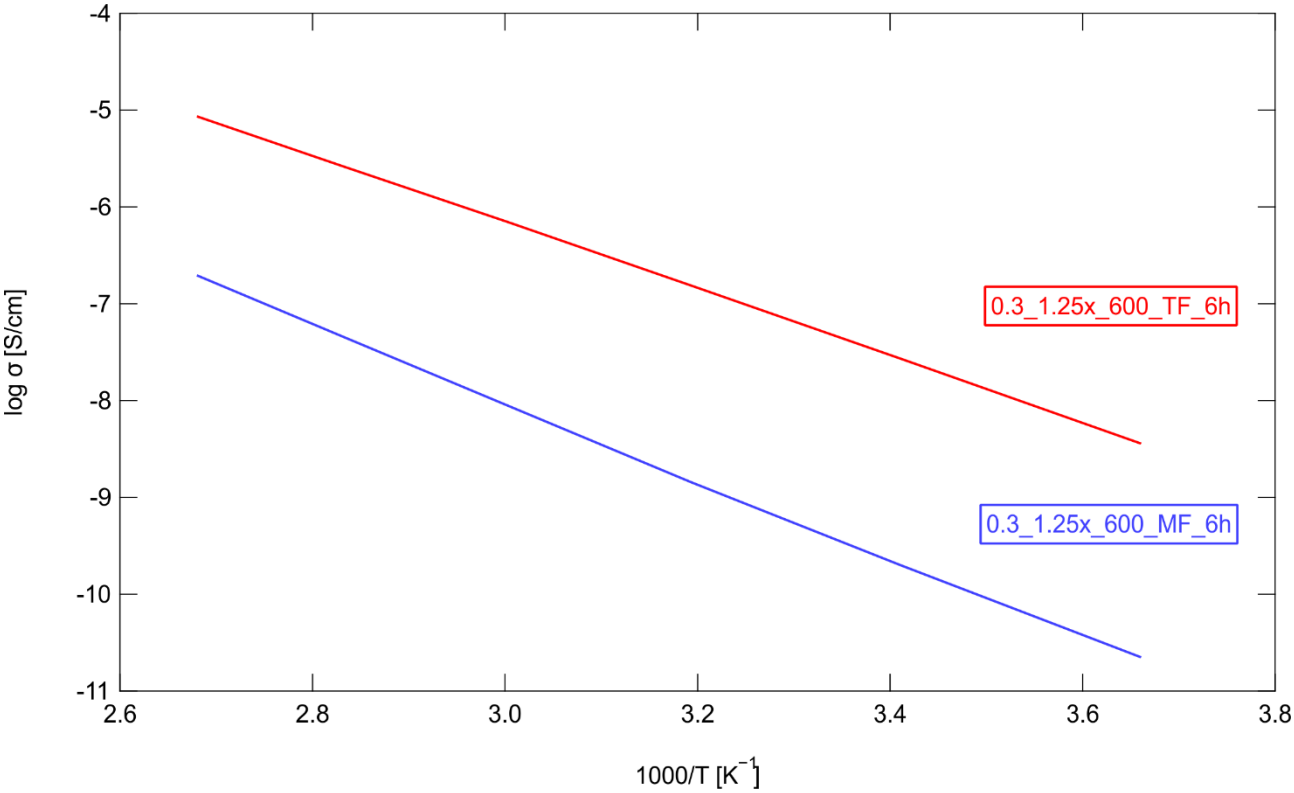

Figure 24 Temperature dependent grain boundary conductivities for sample number 3 and 19

No. 6 – LLZO_0.3_1.25x_1100_TF_6h:

To figure out if covering the pellets with mother powder during sintering influences their ionic conductivity due to reduced Li-loss, a covered and an uncovered pellet of sample 6 were measured via EIS. For the bulk region, there is no significant difference between both samples (figure 26), but albeit the uncovered sample has one of the highest conductivities and lowest activation energies at 20°C it has a low grain boundary ionic conductivity and high activation energy.

No. 4 – LLZO_0.3_1.25x_1000_TF_6h and no. 5 – LLZO_0.3_0.75x_1000_TF_6h:

Sample 4 and 5 only varying in the lithium content showed very similar XRD results with over 85 vol% of cubic LLZO. This can be confirmed with the results of the impedance analysis where the bulk ionic conductivities as well as the activation energies are almost identical (figure 27).

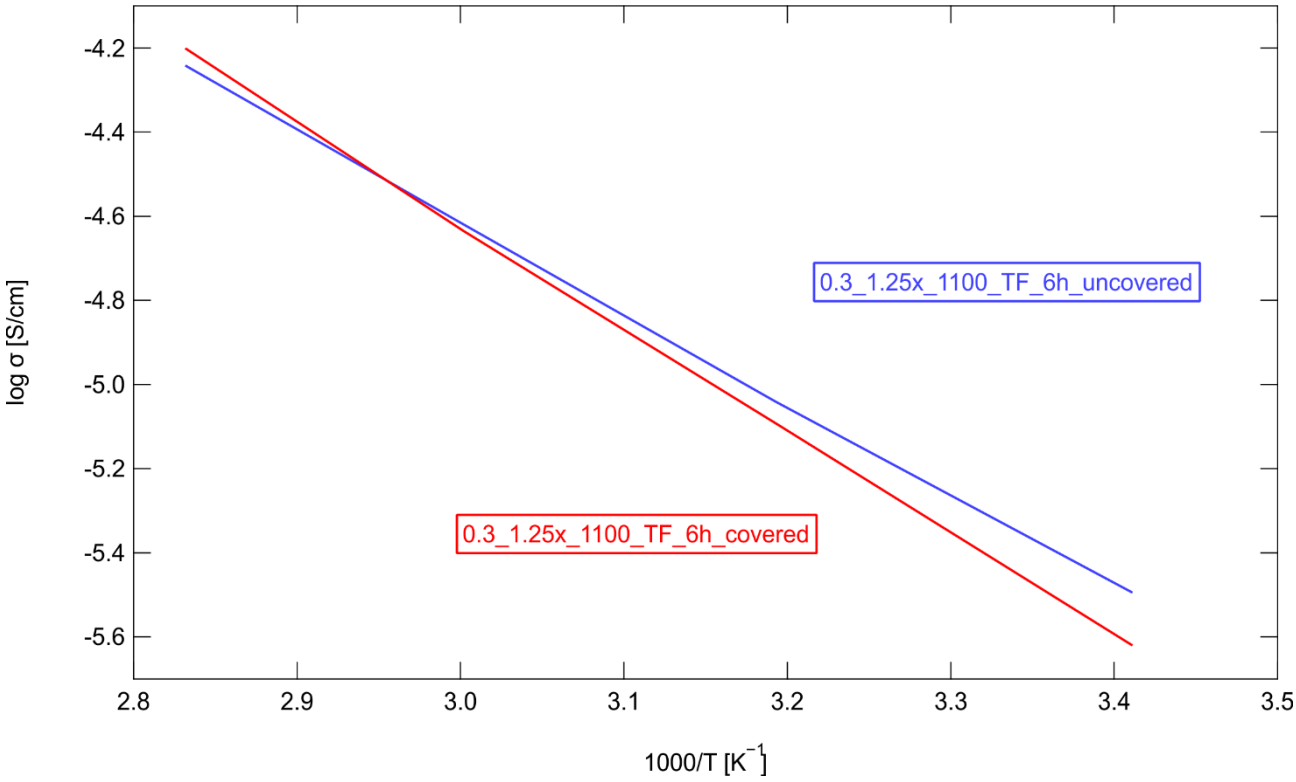

Figure 25 Temperature dependent bulk conductivities for sample number 6 covered with mother powder and without

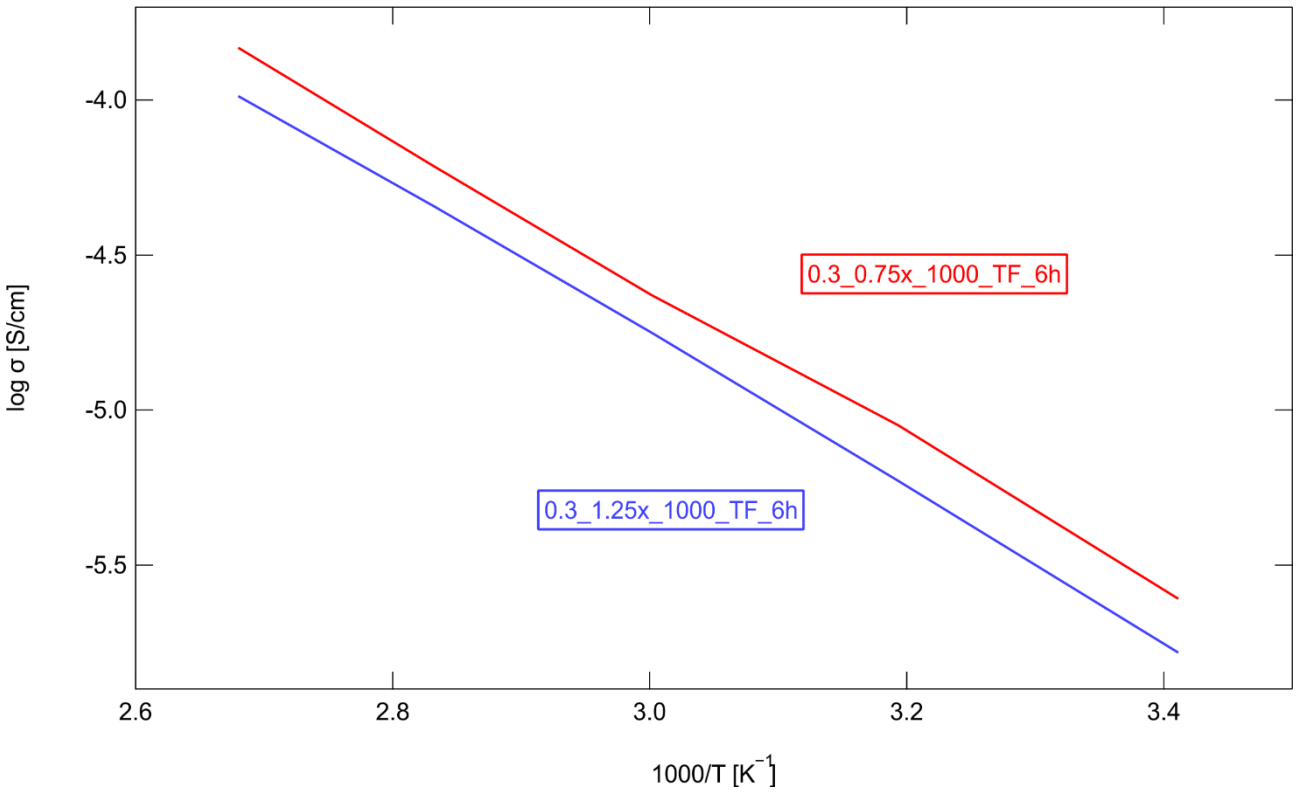

Figure 26 Temperature dependent bulk conductivities for sample number 4 and 5

No. 8 – LLZO_0.2_1.25x_600_TF_6h and no. 9 – LLZO_0.2_1.25x_1000_TF_6h:

Enhancing the temperature from 600° to 1000°C leads to the transformation of a mixture of cubic and tetragonal LLZO as in sample number 8 to cubic modification in sample 9. The ionic bulk conductivity rises from 2.33 x 10^{-7} S cm^{-1} to 1.9 x 10^{-6} S cm^{-1} and the activation drops from 0.52 to 0.46 eV at 20°C (figure 28).

No. 13 – LLZO_0.1_1.25x_1000_TF_6h:

Sample number 13 does not differ significantly from sample number 9 in terms of composition. Nevertheless, it shows a higher ionic conductivity of 5.96 x 10^{-6} S cm^{-1} at 20°C (figure 26).

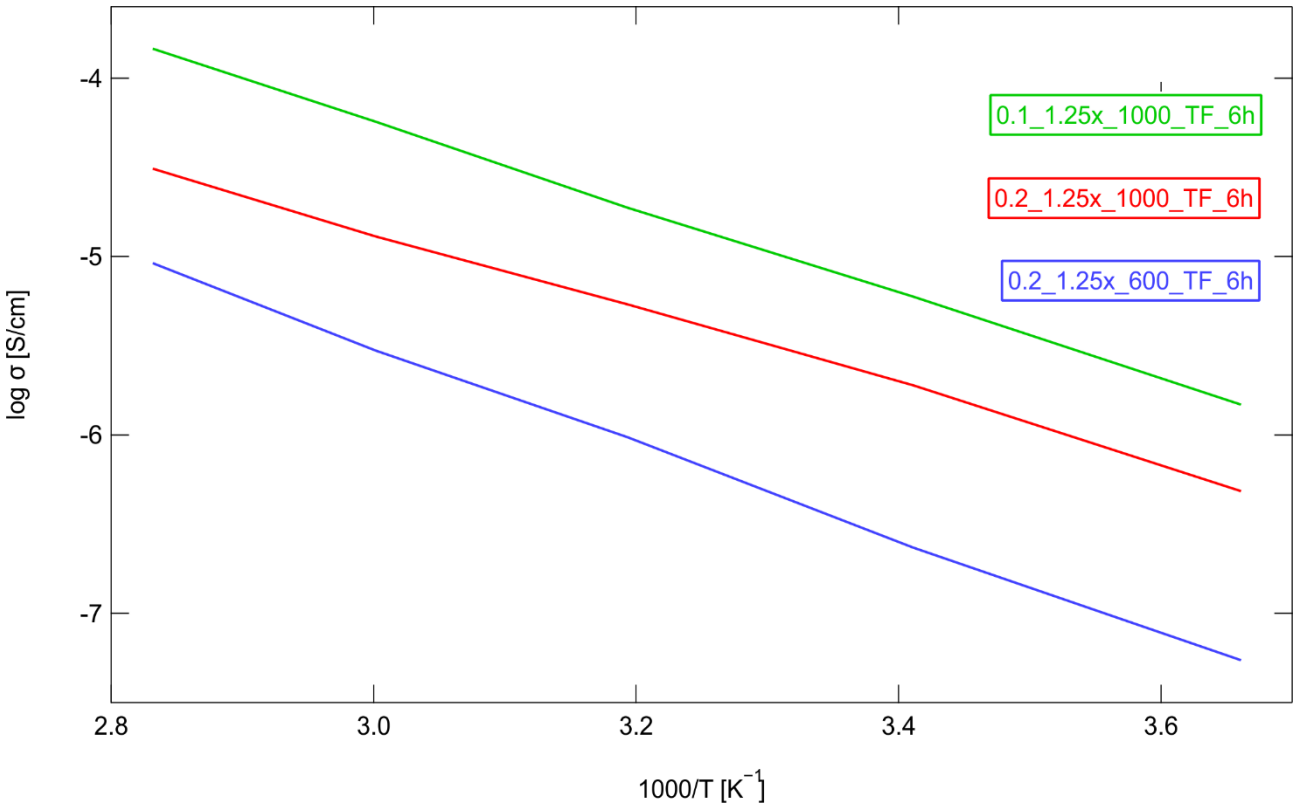

Figure 27 Temperature dependent bulk conductivities for sample number 8, 9 and 13

No. 10 – LLZO_0.3_1.25x_600_TF_6h_Ar and no. 11 –LLZO_0.3_1.25x_600_TF_6h_Ar:

A higher temperature increases the ionic conductivity in the case of LLZO samples sintered in an argon atmosphere (figure 29).

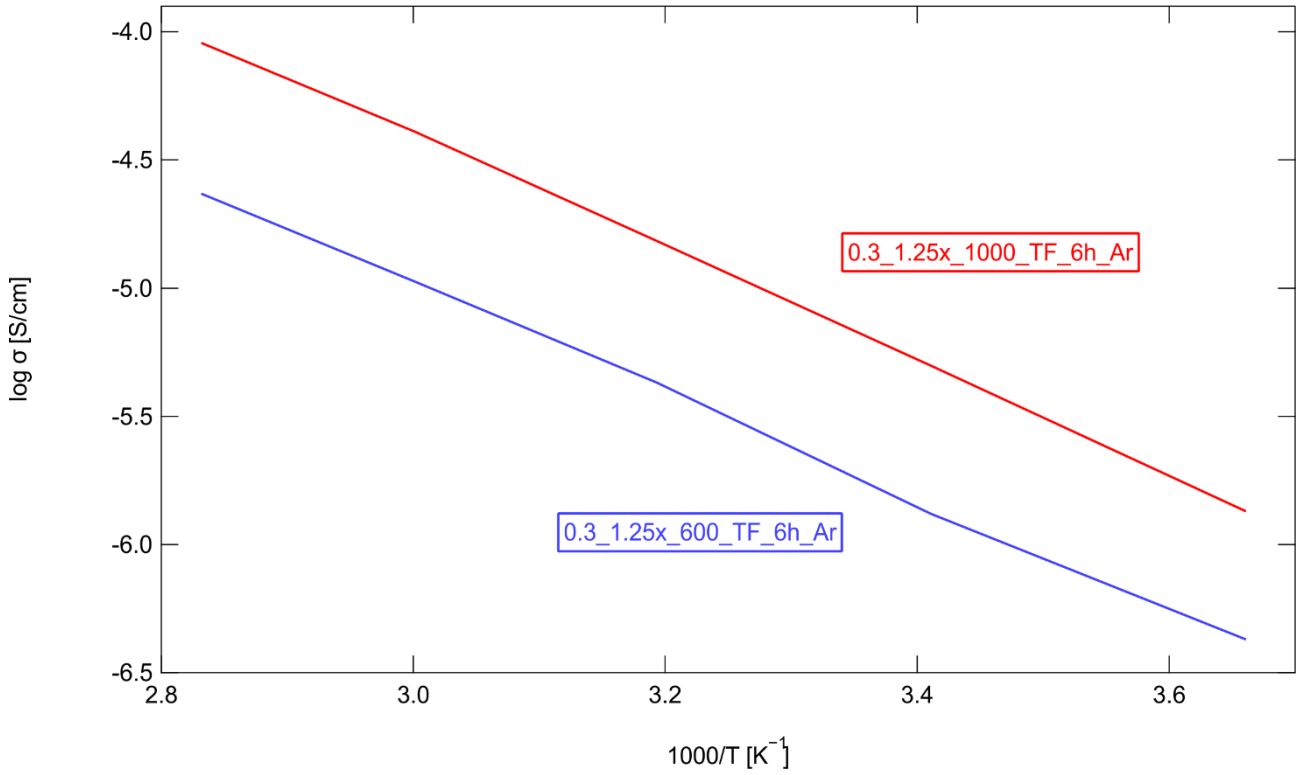

Figure 28 Temperature dependent bulk conductivities for sample number 10 and 11

Table 13 Summary of all activation energies and ionic conductivities at 20°C obtained via EIS measurements

	Bulk		Grain Boundary	
No.	**Activation Energy [eV]**	**Ionic Conductivity [S cm^{-1}]**	**Activation Energy [eV]**	**Ionic Conductivity [S cm^{-1}]**
3	0.42	1.246 x 10^{-6}	0.69	2.713 x 10^{-8}
4	0.49	1.651 x 10^{-6}	0.66	8.274 x 10^{-10}
5	0.5	2.461 x 10^{-6}	0.62	1.476 x 10^{-7}
6 covered	0.5	2.398 x 10^{-6}	0.55	1.083 x 10^{-6}
6 uncovered	0.42	3.203 x 10^{-6}	0.72	6.649 x 10^{-10}
8	0.52	2.334 x 10^{-7}	0.64	1.497 x 10^{-8}
9	0.46	1.898 x 10^{-6}		
10 (Ar)	0.43	1.315 x 10^{-6}	0.64	6.903 x 10^{-8}
11 (Ar)	0.45	4.977 x 10^{-6}	0.55	5.270 x 10^{-7}
13	0.47	5.957 x 10^{-6}	0.57	1.560 x 10^{-6}
19			0.86	1.989 x 10^{-10}
20	0.45	6.513 x 10^{-6}	0.53	1.778 x 10^{-6}

5 Conclusion and Outlook

The aim of this work was to synthesise lithium ion conducting garnet-type metal oxides for future secondary lithium battery applications and to investigate the influence of aluminium doping level, lithium content, sintering temperature and time on the ionic conductivity and composition of the samples. A single step sintering method as well as a multistep sintering procedure were conducted in a tubular and muffle furnace and evaluated. X-ray powder diffraction and electrochemical impedance spectroscopy were chosen for characterisation.

The best results in terms of ionic conductivity were obtained with sample number 20 with a nominal aluminium doping level of x=0.3 sintered at 1000°C for 12 hours under atmospheric conditions. A bulk ionic conductivity of 6.513 x 10^{-6} S cm^{-1} at 20°C and an activation energy of 0.45 eV as well as a grain boundary ionic conductivity of 1.778 x 10^{-6} S cm^{-1} at 20°C and an activation energy of 0.53 eV could be reached. XRPD results showed a composition of over 97 vol% of cubic LLZO.

The influence of an inert argon atmosphere on the sample composition and ionic conductivity was also investigated. It could be shown that the absence of oxygen does not significantly influence the properties at 600°C but at 1000°C impurity formation was absent and a higher ionic conductivity was achieved. So, at higher sintering temperatures there might be a correlation between impurity formation and the presence of oxygen.
The effect of covering the sample pellets with mother powder for electrochemical impedance spectroscopy investigations was also studied. The uncovered sample reached a slightly higher bulk ionic conductivity and lower activation energy and a magnitude of 2 lower grain boundary ionic conductivity than the covered one. Furthermore, it was shown that high energy ball milling alone is not sufficient to produce crystalline cubic lithium-stuffed garnets. Without the addition of aluminium only mixtures of cubic and tetragonal LLZO even at 1100°C could be prepared. So, the possible diffusion of aluminium out of the crucibles is not sufficient to stabilise the cubic modification. Comparing the nominal aluminium content of x = 0.1, 0.2 and 0.3 for single step sintering at 1000°C for 6 hours the doping level of x = 0.1 reached the highest conductivities. The multistep sintering procedure involving high energy ball milling with 2-propanol as solvent did not lead to a satisfactory outcome as only very low cubic LLZO content was obtained and the main phase was the pyrochlore structured $La_2Zr_2O_7$.

In order to improve the ionic conductivity of the lithium stuffed garnets, further characterisation has to be made. The grain sizes, morphology and phase distribution could be evaluated via scanning electron microscopy. ICP-MS should be used for accurate determination of the sample composition. To find the most effective aluminium doping level it must be figured out to which degree the aluminium of the crucibles contributes to the total dopant concentration.

6 List of Figures

7 List of Tables

8 References

(1) Thangadurai, V.; Narayanan, S.; Pinzaru, D. Garnet-type solid-state fast Li ion conductors for Li batteries: Critical review. *Chemical Society reviews* **2014**, *43*, 4714–4727, DOI: 10.1039/c4cs00020j.

(2) *Lithium-ion Batteries: Advances and Applications;* Pistoia, G., Ed.; Elsevier: Amsterdam, 2014.

(3) *The handbook of lithium-ion battery pack design: Chemistry, components, types and terminology;* Warner, J., Ed.; Chemical engineering; Elsevier: Amsterdam, Boston, Heidelberg, 2015.

(4) *Rechargeable lithium batteries: From fundamentals to applications;* Franco, A. A., Ed.; Woodhead publishing series in energy number 81; Elsevier: Amsterdam, 2015.

(5) Bachman, J. C.; Muy, S.; Grimaud, A.; Chang, H.-H.; Pour, N.; Lux, S. F.; Paschos, O.; Maglia, F.; Lupart, S.; Lamp, P. *et al.* Inorganic Solid-State Electrolytes for Lithium Batteries: Mechanisms and Properties Governing Ion Conduction. *Chemical reviews* **2016**, *116*, 140–162, DOI: 10.1021/acs.chemrev.5b00563.

(6) http://pierrehirel.info/recherche_garnet.php?lang=en (accessed April 11, 2017).

(7) Wagner, R.; Redhammer, G. J.; Rettenwander, D.; Senyshyn, A.; Schmidt, W.; Wilkening, M.; Amthauer, G. Crystal Structure of Garnet-Related Li-Ion Conductor Li7-3x Ga x La3Zr2O12: Fast Li-Ion Conduction Caused by a Different Cubic Modification? *Chemistry of materials : a publication of the American Chemical Society* **2016**, *28*, 1861–1871, DOI: 10.1021/acs.chemmater.6b00038.

(8) Kumar, P. J.; Nishimura, K.; Senna, M.; Düvel, A.; Heitjans, P.; Kawaguchi, T.; Sakamoto, N.; Wakiya, N.; Suzuki, H. A novel low-temperature solid-state route for nanostructured cubic garnet Li 7 La 3 Zr 2 O 12 and its application to Li-ion battery. *RSC Adv* **2016**, *6*, 62656–62667, DOI: 10.1039/c6ra09695f.

(9) Dermenci, K. B.; Çekiç, E.; Turan, S. Al stabilized Li7La3Zr2O12 solid electrolytes for all-solid state Li-ion batteries. *International Journal of Hydrogen Energy* **2016**, *41*, 9860–9867, DOI: 10.1016/j.ijhydene.2016.03.197.

(10) Irvine, J. T. S.; Sinclair, D. C.; West, A. R. Electroceramics: Characterization by Impedance Spectroscopy. *Adv. Mater.* **1990**, *2*, 132–138, DOI: 10.1002/adma.19900020304.

(11) Rangasamy, E.; Wolfenstine, J.; Sakamoto, J. The role of Al and Li concentration on the formation of cubic garnet solid electrolyte of nominal composition Li7La3Zr2O12. *Solid State Ionics* **2012**, *206*, 28–32, DOI: 10.1016/j.ssi.2011.10.022.

(12) *Lithium-ion batteries: Advanced materials and technologies;* Liu, H.; Zhang, J.; Yuan, X., Eds.; Green chemistry and chemical engineering; CRC Press: Boca Raton, 2012.

(13) *Handbook of Battery Materials*. Volume 1; Daniel, C.; Besenhard, J. O., Eds.; Wiley: Weinheim, 2012.

(14) http://www.electrochem.org/exploding-hoverboards-explained (accessed April 8, 2017).

(15) *Handbook of Battery Materials*. Volume 2; Daniel, C.; Besenhard, J. O., Eds.; Wiley: Weinheim, 2012.

(16) *Elektrochemie;* Hamann, C. H.; Vielstich, W., Eds., 4., vollständig überarbeitete und aktualisierte Auflage; Wiley-VCH-Verlag GmbJ &Co. KGaA: Weinheim, 2005.

(17) Xu, K. Nonaqueous Liquid Electrolytes for Lithium-Based Rechargeable Batteries. *Chemical reviews* **2004**, *104*, 4303–4418, DOI: 10.1021/cr030203g.

(18) *Handbook of solid state batteries & capacitors;* Munshi, M. Z. A., Ed.; World Scientific Pub. Co: Singapore, River Edge, N.J, 1995.

(19) Thangadurai, V.; Kaack, H.; Weppner, W. J. F. Novel Fast Lithium Ion Conduction in Garnet-Type Li 5 La 3 M 2 O 12 (M = Nb, Ta). *Journal of the American Ceramic Society* **2003**, *86*, 437–440, DOI: 10.1111/j.1151-2916.2003.tb03318.x.

(20) Murugan, R.; Thangadurai, V.; Weppner, W. Fast lithium ion conduction in garnet-type Li(7)La(3)Zr(2)O(12). *Angewandte Chemie (International ed. in English)* **2007**, *46*, 7778–7781, DOI: 10.1002/anie.200701144.
(21) Rettenwander, D.; Redhammer, G.; Preishuber-Pflugl, F.; Cheng, L.; Miara, L.; Wagner, R.; Welzl, A.; Suard, E.; Doeff, M. M.; Wilkening, M. *et al.* Structural and Electrochemical Consequences of Al and Ga Cosubstitution in Li7La3Zr2O12 Solid Electrolytes. *Chemistry of materials : a publication of the American Chemical Society* **2016**, *28*, 2384–2392, DOI: 10.1021/acs.chemmater.6b00579.
(22) Sakamoto, J.; Rangasamy, E.; Kim, H.; Kim, Y.; Wolfenstine, J. Synthesis of nano-scale fast ion conducting cubic Li7La3Zr2O12. *Nanotechnology* **2013**, *24*, 424005, DOI: 10.1088/0957-4484/24/42/424005.
(23) Xu, B.; Duan, H.; Xia, W.; Guo, Y.; Kang, H.; Li, H.; Liu, H. Multistep sintering to synthesize fast lithium garnets. *Journal of Power Sources* **2016**, *302*, 291–297, DOI: 10.1016/j.jpowsour.2015.10.084.
(24) Düvel, A.; Kuhn, A.; Robben, L.; Wilkening, M.; Heitjans, P. Mechanosynthesis of Solid Electrolytes: Preparation, Characterization, and Li Ion Transport Properties of Garnet-Type Al-Doped Li 7 La 3 Zr 2 O 12 Crystallizing with Cubic Symmetry. *J. Phys. Chem. C* **2012**, *116*, 15192–15202, DOI: 10.1021/jp301193r.
(25) *Impedance spectroscopy: Applications to electrochemical and dielectric phenomena;* Lvovich, V. F., Ed.; Wiley: Hoboken, N.J, 2012.
(26) *Grundlagen der Elektrochemie;* Schmickler, W., Ed.; Vieweg Lehrbuch Physikalische Chemie; Vieweg: Braunschweig, 1996.
(27) *Electrochemical methods: Fundamentals and applications;* Bard, A. J.; Faulkner, L. R., Eds., 2. ed.; Wiley: Hoboken, NJ, 2001.
(28) *Analytical and physical electrochemistry;* Girault, H. H., Ed.; Fundamental sciences Chemistry; EPFL: Lausanne, Switzerland, New York, 2004.
(29) *Introduction to X-Ray Powder Diffractometry;* Jenkins, R.; Snyder, R., Eds.; Chemical Analysis; Wiley: New York, 1996.
(30) *Anorganische Chemie;* Riedel, E.; Janiak, C., Eds., 8. Aufl.; Studium; de Gruyter: Berlin, 2011.
(31) http://www-structmed.cimr.cam.ac.uk/Course/Basic_diffraction/Diffraction.html (accessed April 8, 2017).